Supporting Information

for

Atomic Origin of the Autocatalytic Reduction of Monoclinic CuO in a Hydrogen Atmosphere

Xianhu Sun,[1, ∇] Dongxiang Wu,[1, ∇] Wenhui Zhu,[1] Xiaobo Chen,[1] Renu Sharma,[2] Judith C. Yang,[3] Guangwen Zhou[1*]

[1.] Department of Mechanical Engineering & Materials Science and Engineering Program, State University of New York, Binghamton, New York 13902, United States

[2.] Nanoscale Device Characterization Division, National Institute of Standards and Technology, Gaithersburg, Maryland 20899, United States

[3.] Department of Chemical and Petroleum Engineering, University of Pittsburgh, Pittsburgh, Pennsylvania 15261, United States

∇ These authors contributed equally to the work

* Correspondence to: gzhou@binghamton.edu

This file includes:

Other Supplementary Materials for this manuscript include the following:

Experimental Methods

In-situ environmental TEM (ETEM) experiments. In-situ TEM experiments included two steps, starting from the in-place CuO formation by the oxidation of Cu, followed by CuO reduction by switching the gas flow from O_2 to H_2, both which were conducted in a dedicated objective-lens aberration-corrected ETEM equipped with a gas manifold that enables introducing various gases to the specimen area.[1-2] Commercial TEM Cu grids (99.9 % purity) were used as the original specimen in the in-situ ETEM experiments. The Cu grids were first thoroughly rinsed in deionized water followed by ultrasonication in acetone for 10 min, and then treated by plasma cleaning before loading into the TEM column. The Cu grids were further cleaned inside the TEM by heating to 400 °C in a H_2 gas flow to remove any native oxide. The resulted Cu grids were then directly oxidized at 400 °C to form a bulk CuO layer inside the TEM by flowing O_2 gas at the pressure of ≈ 0.5 Pa in the specimen area of the TEM column. The CuO formed from the thermal oxidation process is of both high crystallinity due to the high temperature and high purity for the elimination of any other chemical intermediaries. After the oxidation step, the specimen was then cooled down to 300 °C and the O_2 flow was stopped. Remaining oxygen in the TEM column was evacuated before H_2 was introduced to the specimen region. The pressure of the H_2 gas flow was maintained at ≈ 0.53 Pa, and the specimen temperature was maintained at 300 °C during the H_2 flow. This two-step process of the in-place sample preparation by oxidation and subsequent in-situ observation of the reaction of the oxide with H_2 has the advantage of minimizing potential sample contamination. Acceleration voltage and e-beam dosage we applied were 300 keV and ≈ 1.1×10^5 $e \cdot nm^{-2} \cdot s^{-1}$, respectively. Real-time movies were recorded with a frame rate of 2 or 5 frames/s. The image frames were aligned to compensate the thermal drift.

To minimize any potential e-beam induced oxide reduction, the e-beam was blanked except for data acquisition. In addition, our TEM observations by blanking and un-blanking the electron beam confirmed that the electron beam effect has a negligible effect on the observed autocatalytic oxide reduction.

DFT Calculations. Periodic DFT calculations were performed using the Vienna Ab initio Simulation Package (VASP).[3-5] Perdew, Burke, and Ernzerhof (PBE) generalized gradient approximation (GGA)[6] and projector augmented-wave (PAW)[7] potential were performed to describe the electron–electron exchange and core-electron potential separately. Heyd–Scuseria–Ernzerhof (HSE06) hybrid functional and PBE were both applied in our calculations (Supplementary Table 1). The oxygen vacancy diffusion barriers along the same pathways with the use of these two functionals are comparable, suggesting that PBE provides the sufficient accuracy in our DFT calculations. DFT + U was employed in our DFT calculations to include the strong correlation effect among the partially filled Cu 3d states in CuO.[8] According to the previous study, the values of U and J were selected as 7 and 0 eV for CuO, respectively.[9-10] To test the cut-off energy, we used the energies of 400 and 500 eV to calculate hydrogen adsorption energies. Their small difference of 0.05 eV suggested that the cut-off energy of 400 eV was sufficient, so the plane-wave cutoff energy was set to be 400 eV for all the calculations. Spin-polarized calculations were performed since CuO has an antiferromagnetic ground state. The Brillouin-zone integration was performed using ($8 \times 8 \times 8$) K-point meshes based on Monkhorst-Pack grids. A CuO supercell with 16 O and 16 Cu atoms was established for DFT calculations. CuO has the monoclinic symmetry with space group $C2/c1$ (a=0.4939 nm, b=0.3674 nm, c=0.5127 nm, and β=96.152°).[11] The structural optimization was performed using DFT+U with all force components

acting on the atoms less than 0.15 eV nm^{-1}. Each atom has four nearest neighbors of the other kind: Cu atom is located in the center of an O parallelogram. O atom, in turn, is surrounded by a distorted tetrahedron of Cu atoms. Lengths of the a-, b-, and c-axes of the supercell for simulations are fixed since the CuO-superlattice and the parent phase of CuO are fully coherent, as shown in Figure 1c and f. To study O vacancy formation and H adsorption on the CuO $(\bar{1}10)$ surface, a (2 × 2) surface supercell expansion was used and a (4 × 4) surface supercell was also used to further check the results for O vacancy formation. We used periodic slabs with a vacuum spacing 1.2 nm to model the CuO $(\bar{1}10)$ surface, and the slab was composed of 5 atomic layers with the bottom two layers fixed, while the top three layers were free to relax. A (2 × 2) supercell was used for modeling the CuO-superlattice structure with 25 % O vacancies. We also carried out a convergence test of the K-points mesh by comparing the total energy difference using (4×4×1) and (8×8×1) meshes. Our results showed that sufficient convergence is reached using the (4×4×1) mesh, since the (8×8×1) mesh gave a total energy difference of less than 0.02 eV. Thus, the Brillouin zone was selected as 4 × 4 × 1 and 4 × 4 × 4 k-point grids for the surface and bulk models, respectively. We used $E_{ads} = \frac{1}{N_H}(E^{tot}_{H/CuO} - E_{ref} - \frac{No}{2}E_{H_2})$ and $E_{vac} = E^{tot}_{slab/vac} - E_{atom} - E_{slab}$ to describe the H adsorption and vacancy formation energies, respectively. We also modeled the diffusion pathways and associated energy barriers by using the nudged elastic band (NEB) method with five intermediate images between the initial state and the final state[12]. All the atomic structures were visualized using the Visualization for Electronic and Structure Analysis (VESTA).

HRTEM and diffractogram simulations. The DFT-relaxed atomic structure models of CuO and CuO-superlattice were used as input files for HRTEM image and diffractogram

simulations. HRTEM image simulations were performed using the multi-slice method with the parameters carefully matched to the experimental conditions (accelerating voltage: 300 keV, the spherical aberration: 0.001 mm, defocus: -1 nm, thickness: 32 nm (for images in Figure 1), and Debye-Waller factors: 0.005 for both O and Cu atoms).[2] The simulated HRTEM images were processed by adding shot/Poisson noise (counting noise) because the counted electrons in the pixels followed the Poisson distribution. The frozen phonon model was applied to reduce the elastic scattering and increase the background intensity.

Measurement of reduction kinetics. The reduction kinetics is measured from in situ TEM images by temporally tracking the shrinkage of the projection area of the oxide and lateral length of the atomic layers as a function of the retraction motion of atomic steps. This is performed by using the selection brush tool in ImageJ software. This tool allows to adjust the shape of an area selection using a circular brush. The pixel size is 0.02 nm×0.02 nm (same as the pixel size of the TEM images). The error bars in Figures 2 and 3 represent the standard deviation uncertainties based on multiple measurements. The value of the error bars can be relatively large (up to multiple d-spacing, e.g., d($\bar{1}\bar{1}2$) ~ 0.2 nm) because the relatively low image contrast of the leading edge (atomic steps) of atomic layers result in some large uncertainties in locating the position of the atomic steps.

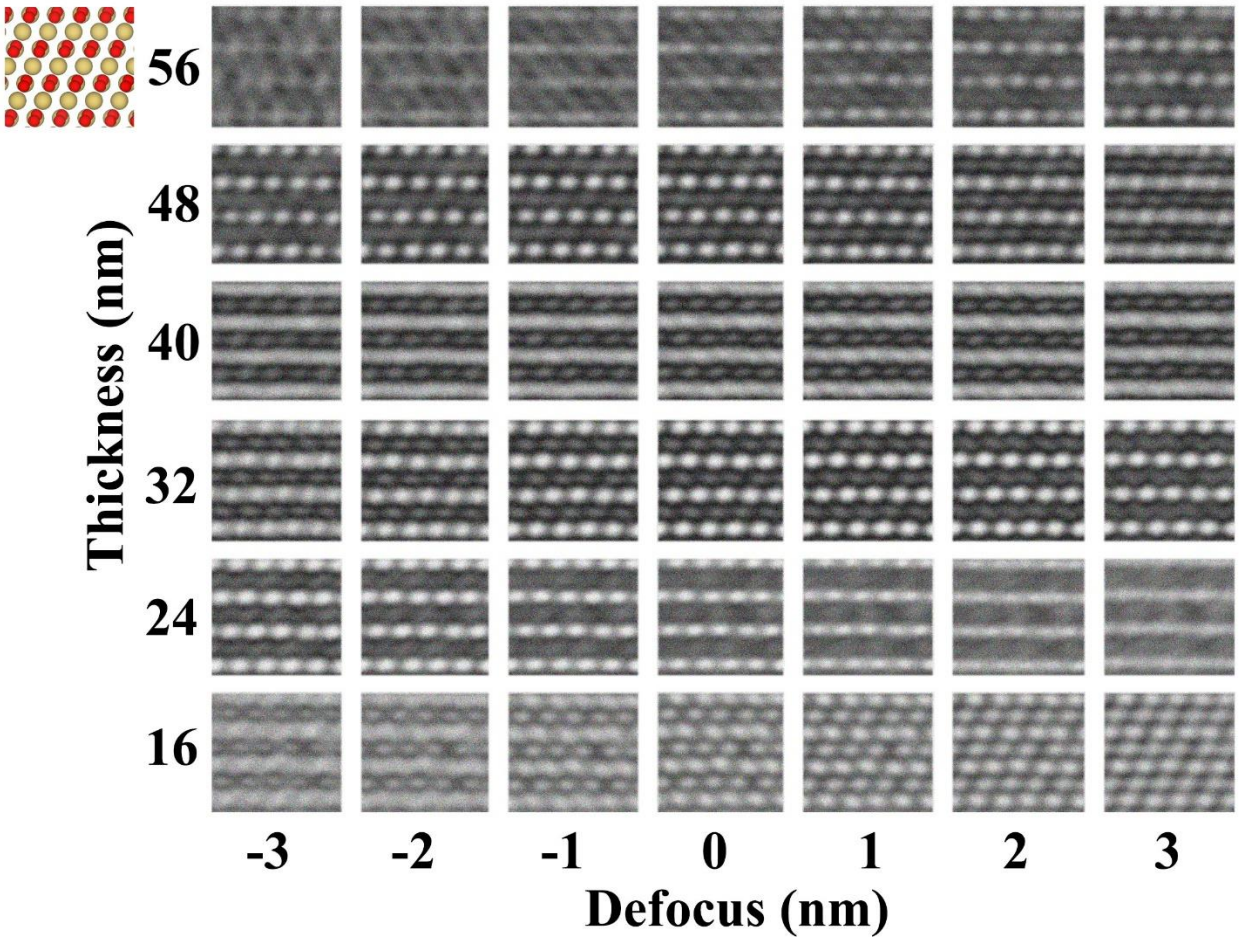

Figure S1. HRTEM image simulations for the stoichiometric CuO viewed along the $[\bar{1}\bar{1}\bar{1}]$ direction. The input atomic model for the simulation is shown in the upper-left corner, where the yellow and red balls represent Cu and O, respectively. Specimen thickness increases from bottom to top and defocus increases from left to right.

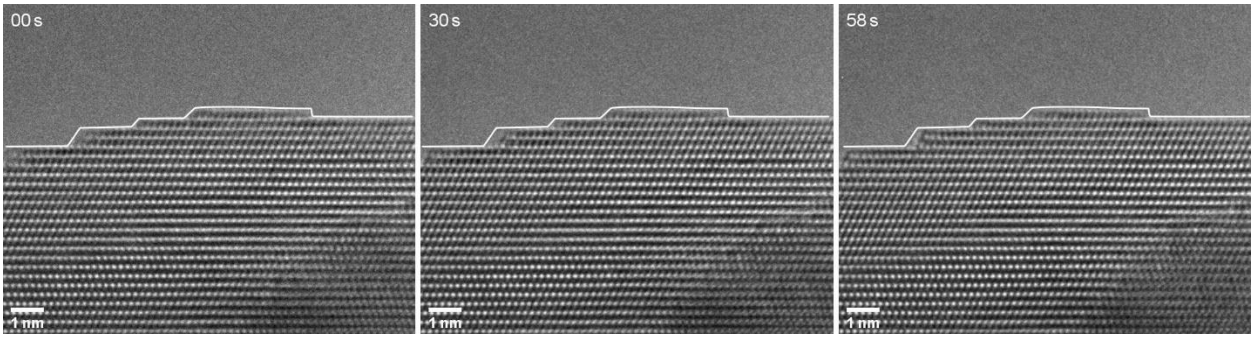

Figure S2. Stable surface configuration of CuO in vacuum at 300 ℃ (from Supplementary Movie S1). Comparison of the initial surface location (marked by white line) with that at 30 s and 58 s indicates the CuO surface is stable in vacuum at 300 ℃ within a period of ≈ 60 s. This reveals the surface step retraction of the oxide in H_2 flow is predominated by H_2 molecules attack.

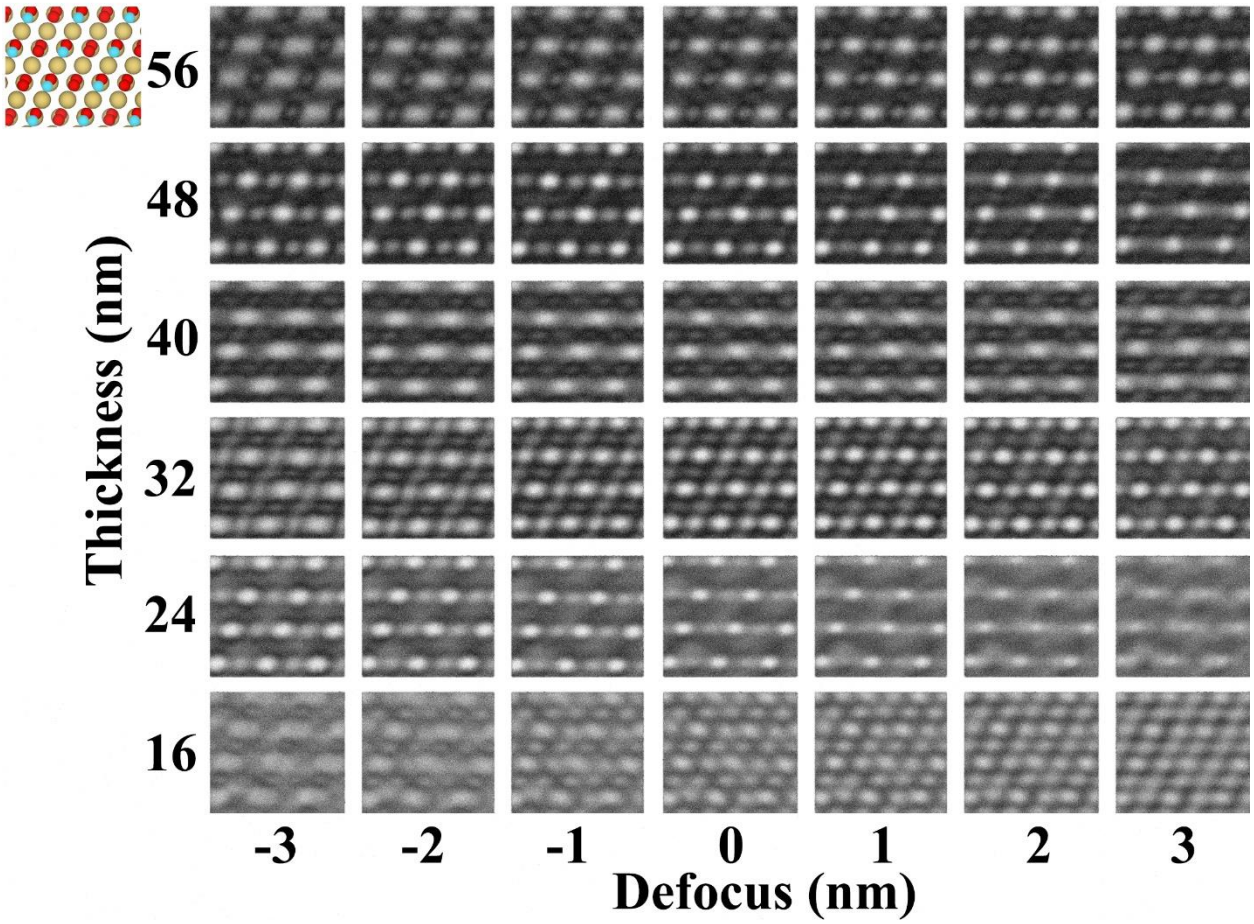

Figure S3. HRTEM image simulations for the CuO superstructure with 25 % O vacancies viewed along the $[\bar{1}\bar{1}\bar{1}]$ direction. The input atomic model (same as Figure 1f) for the simulation is shown in the upper-left corner, where the yellow, red, and cyan balls represent Cu, O, and O vacancy, respectively. In this model, 50 % O lose in every other Cu-O column of the CuO lattice. Specimen thickness increases from bottom to top and defocus increases from left to right.

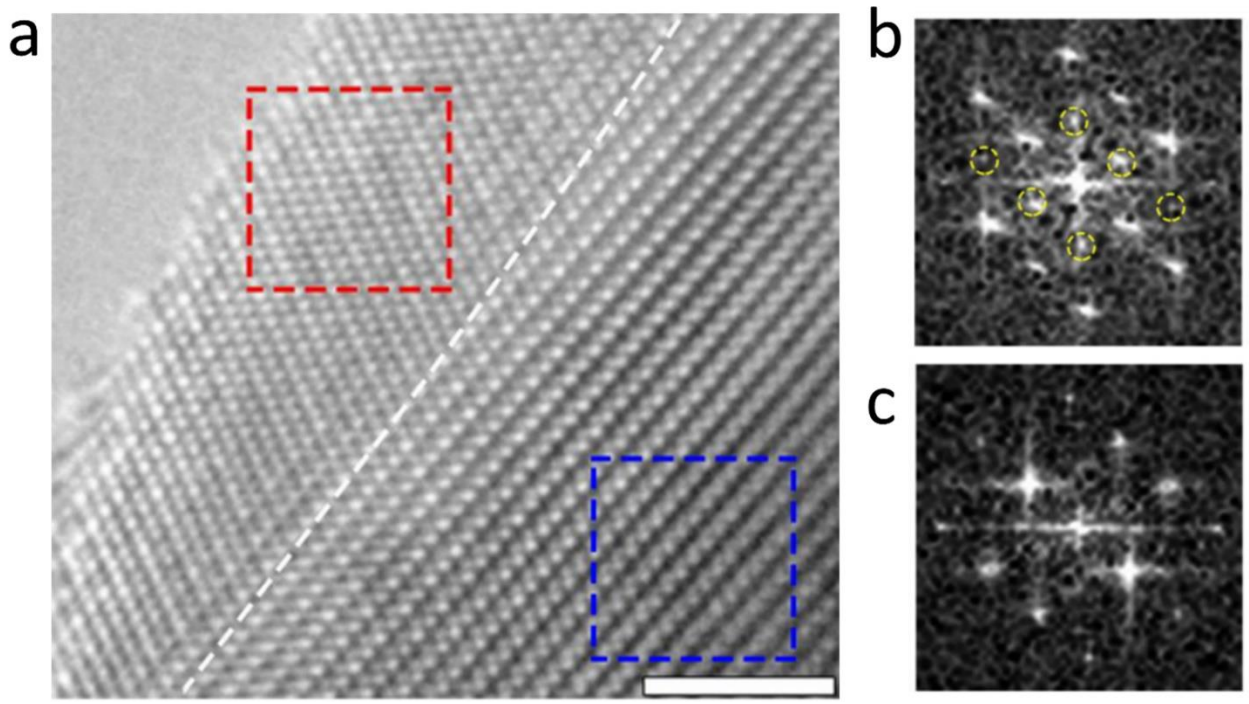

Figure S4. (a) HRTEM image showing a coherent interface (marked by the white dashed line) between CuO and the partially reduced CuO superlattice. (b-c) FFT Diffractograms of the regions marked with the red and blue dashed squares in (a), corresponding to the CuO superstructure and the parent CuO, respectively. The superlattice spots in (b) are marked by yellow dashed circles. Scale bar in (a), 2 nm

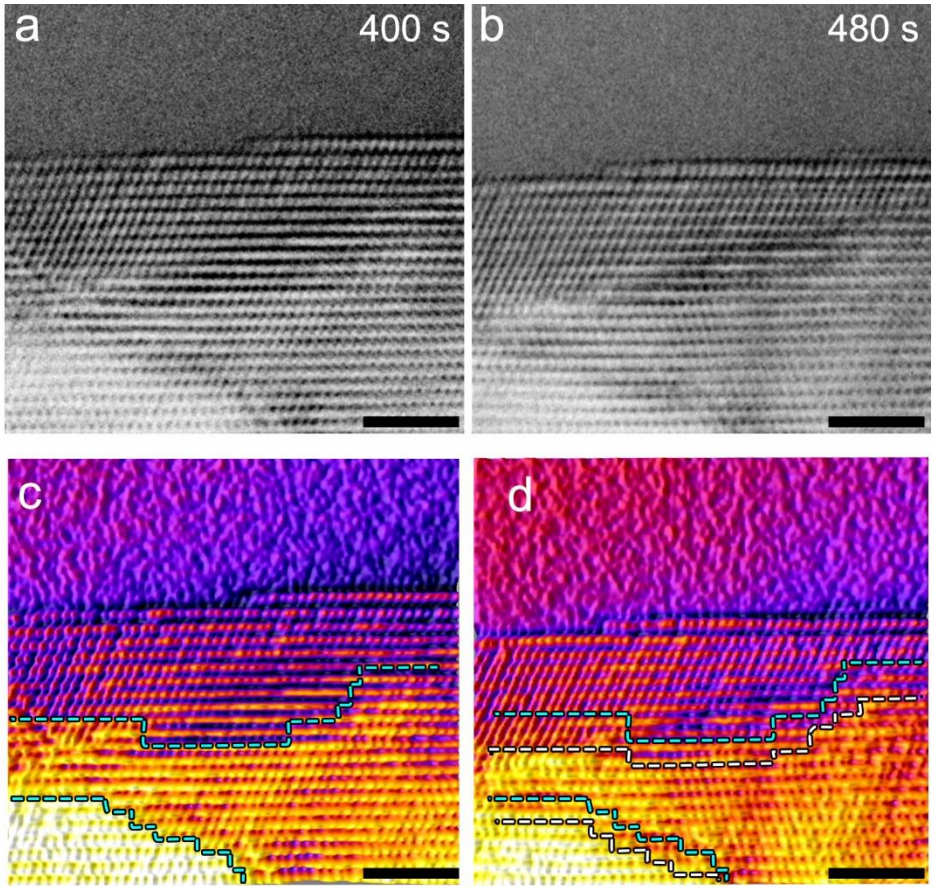

Figure S5. Time-resolved planar-view in-situ TEM images showing the retraction motion of atomic steps on the planar surface during the CuO reduction at T=300 ℃ and pH_2=0.5 Pa. These in-situ TEM images are extracted from supplementary in-situ TEM movie 2. The pseudo colors are applied in (c, d) to guide the eye and show the atomic steps on the planar surface. The dashed cyan lines in (d) are the superimposed trace of the position and profile of the surface steps at t=400 s in (c), showing the retraction movement of the surface steps during the oxide reduction. Scale bar, 2 nm

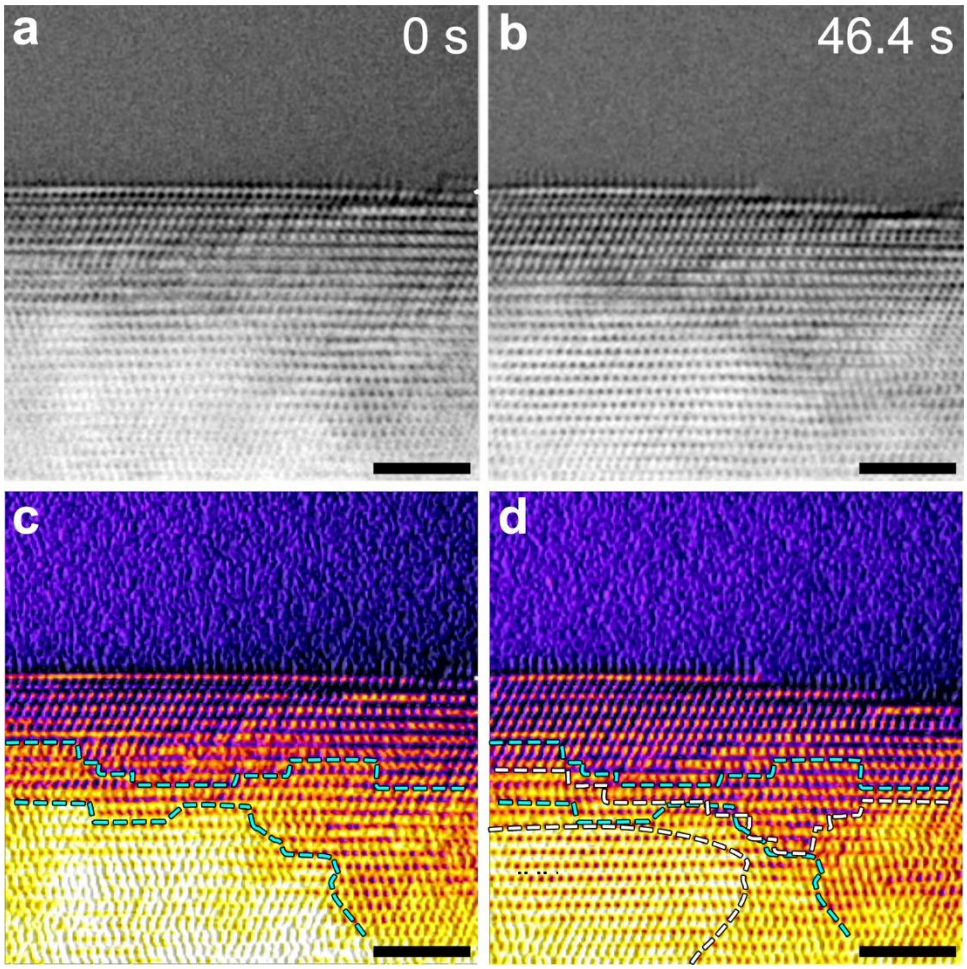

Figure S6. Time-resolved planar-view in-situ TEM images showing the retraction motion of atomic steps on the planar surface during the CuO reduction at T=300 ℃ and pH_2=0.5 Pa. These in-situ TEM images are extracted from supplementary in-situ TEM movie 3. The pseudo colors are applied in (c, d) to guide the eye and show the atomic steps on the planar surface. The dashed cyan lines in (d) are the superimposed trace of the position and profile of the surface steps at t=0 s in (c), showing the retraction movement of the surface steps during the oxide reduction. Scale bar, 2 nm

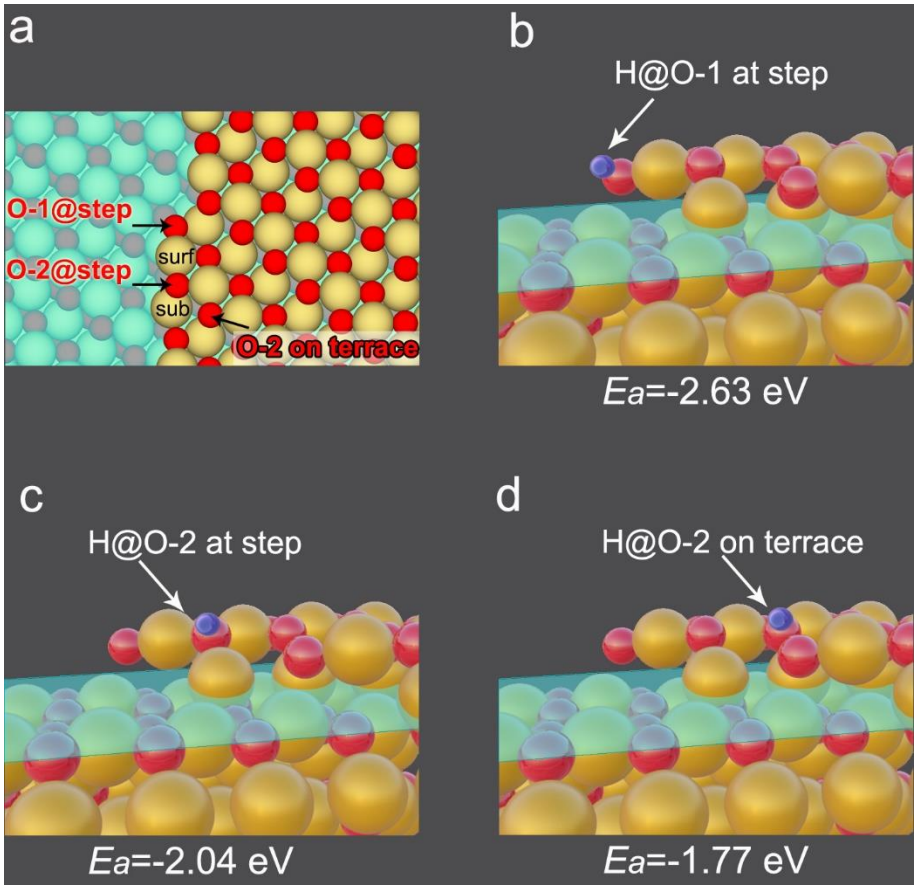

Figure S7. Top and perspective views of the atomic configuration of the Cu-O/Cu bilayer atomic step and the adjacent terrace sites for DFT modeling of H adsorption sites of the step edge, revealing the preferred H adsorption by the O atom at the step edge. (a) Top view of CuO step model showing the step edge has two nonequivalent oxygen (O-1 and O2). The abbr. "surf" and "sub" indicate the step edge Cu in the surface and subsurface. (b) H adsorption by O-1 at the step edge, resulting in an adsorption energy of -2.63 eV. (c) H adsorption by O-2 at the step edge, resulting in an adsorption energy of -2.04 eV. (d) H adsorption by the adjacent terrace O atom with an adsorption energy of -1.77 eV. Yellow, red, and purple balls represent Cu, O and H atoms, respectively.

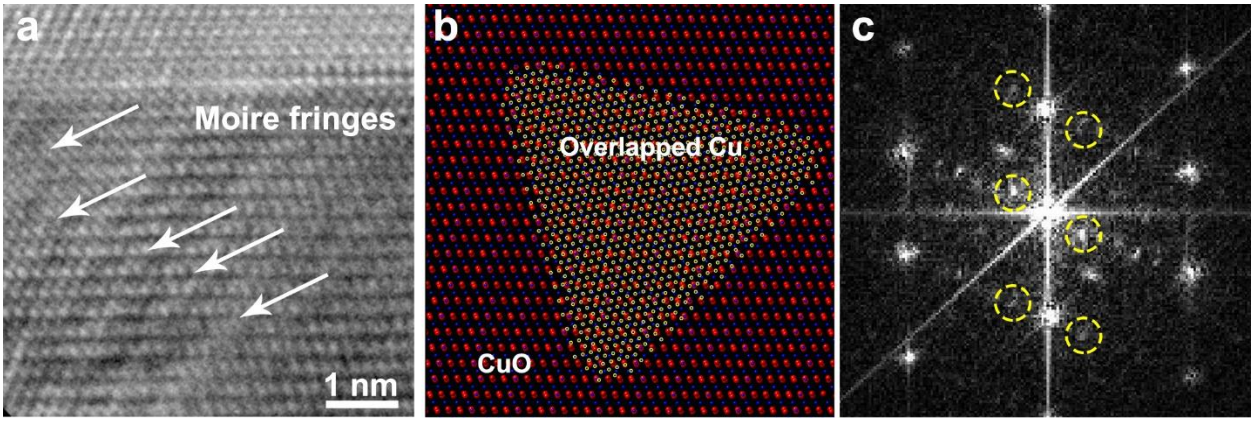

Figure S8. Aggregation of Cu atoms freed from the retraction motion of surface steps on CuO. Under the H_2 gas flow, CuO reduction occurs in the form of the retraction motion of Cu-O/Cu bilayer atomic steps. Cu atoms freed from the step-edge detachment diffuse to inner surface regions of the oxide, and subsequently aggregate into a thin Cu film on the parent CuO. (a) The overlapping of the Cu thin layer with the CuO substrate results in the Moiré fringe contrast, as marked by white arrows in the HRTEM image. (b) Schematic illustrating the formation of a Cu overlayer on CuO, where the yellow balls represent aggregated Cu atoms. (c) Diffractogram of the HRTEM image in (a), showing the double diffraction reflections (yellow dashed circles) due to the overlapped Cu and CuO lattices.

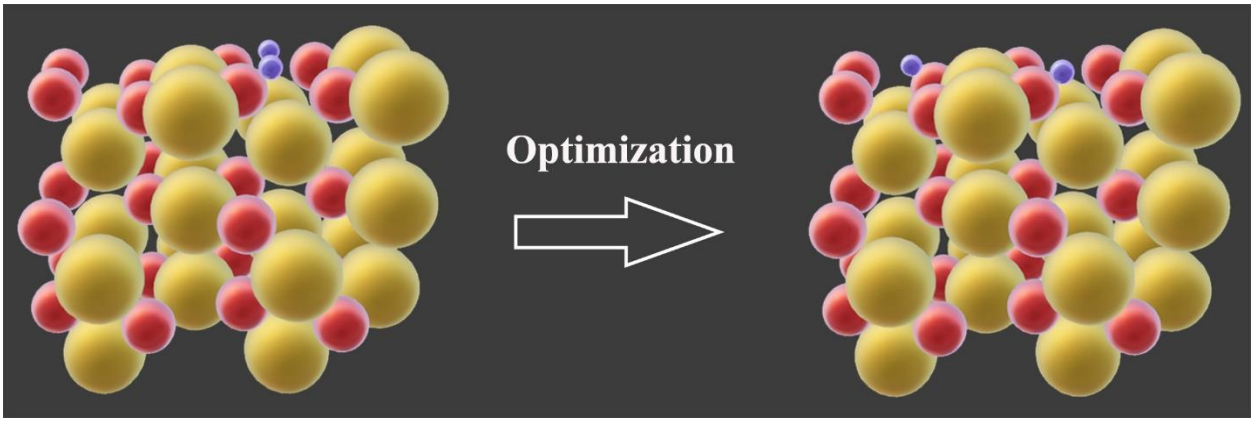

Figure S9. DFT modeling of the adsorption of H_2 molecules on CuO $(\bar{1}10)$, showing the spontaneous dissociation of the H_2 molecule into two atomic H. One H_2 molecule is placed in the vacuum, ≈ 0.02 nm above the top of the lattice O at the CuO $(\bar{1}10)$ surface (left). After the structure relaxation, the H_2 molecule is observed to dissociate spontaneously into two H atoms that bond with the adjacent lattice O to form two OH groups (right). Yellow, red, and purple balls represent Cu, O and H atoms, respectively.

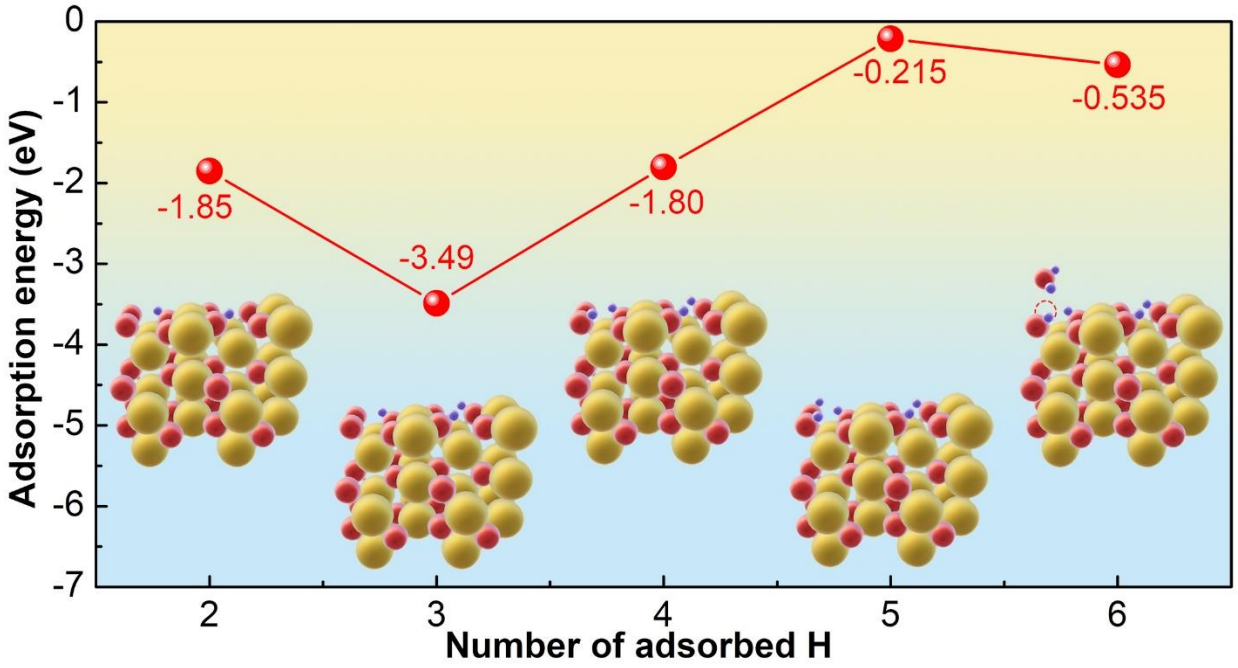

Figure S10. DFT modeling of the H_2O formation by progressive H adsorption. The insets show the minimum-energy configurations upon the sequential H adsorption at the energetically favorable sites of the CuO $(\bar{1}10)$ surface. The continued adsorption of H atoms gives rise to the formation of OH groups that remain stable at the surface until reaching 0.625 monolayer of the surface coverage, at which the repulsive forces between adjacent hydroxyls make the top site of hydroxyls more favorable than the remaining sites of lattice O to adsorb further H atoms. Our calculations show that the H adsorption on top of the hydroxyls produces the formation of H_2O molecules that desorb spontaneously from the surface without requiring any barriers. The H_2O desorption results in the loss of lattice O with the concomitant formation of O vacancies at the oxide surface. Yellow, red, and purple balls represent Cu, O, and H, respectively. The red dashed circle corresponds to the O vacancy resulting from the desorption of the H_2O molecule.

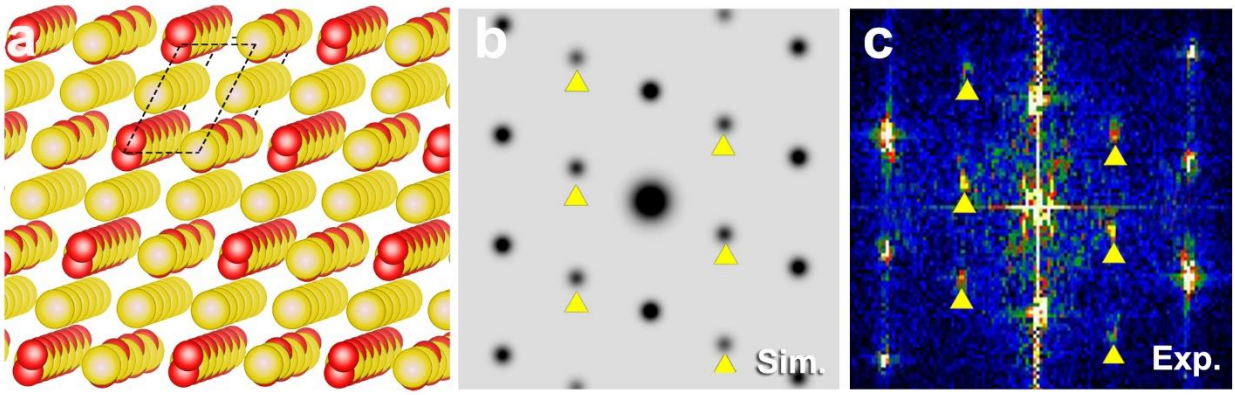

Figure S11. CuO-superlattice resulting from the self-ordering of O vacancies. (a) Extended view of the CuO-superlattice (shown in Figure 4h) with 25 % O vacancies, viewed along the $[\bar{1}\bar{1}\bar{1}]$ direction. (b) Simulated electron diffraction pattern based on the CuO-superlattice in (a). (c) Diffractogram of the HRTEM images of the CuO-superlattice in the subsurface region of the partially reduced CuO samples. Yellow triangles in (b, c) correspond to the superlattice diffraction spots resulting from the self-ordering of O vacancies in the CuO lattice, indicating the good match between the simulated (b) and experimental (c) diffractograms. Yellow and red balls represent Cu and O, respectively.

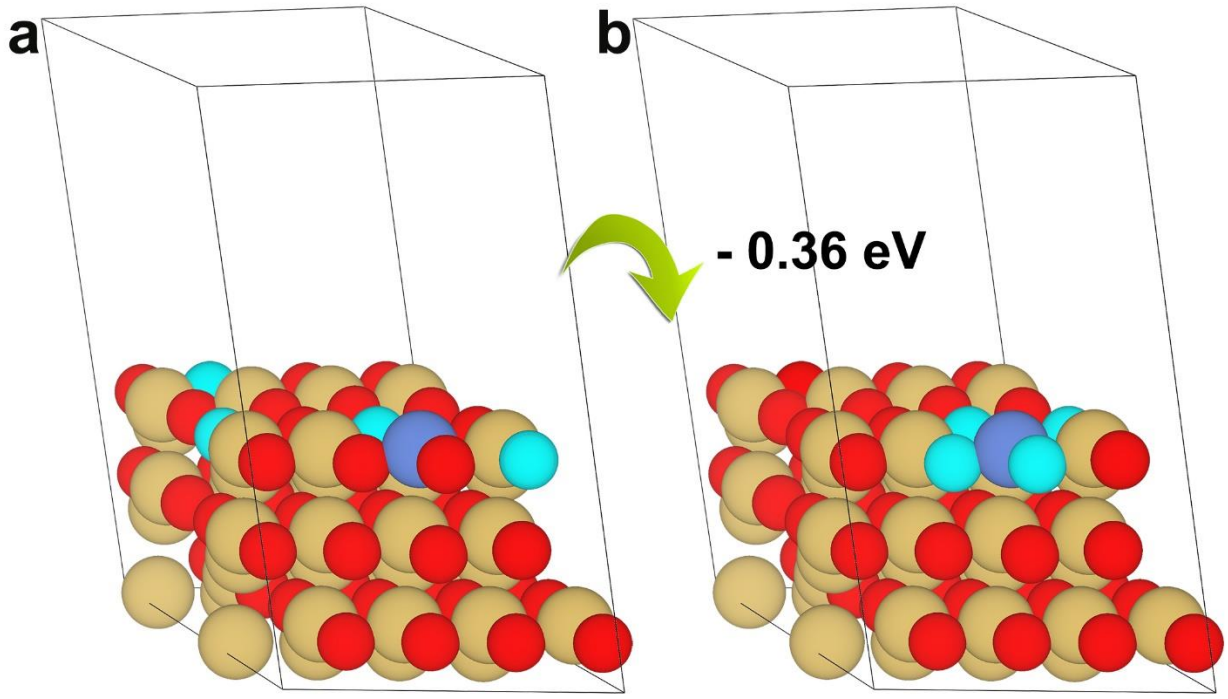

Figure S12. DFT modeling of the surface clustering of O vacancies. (a) Atomic configuration showing four separated O vacancies (cyan balls) and one Cu vacancy (blue ball). (b) The coalescence of the four O vacancies and one Cu vacancy results in a reduced system energy by 0.36 eV. Yellow, red, blue and cyan balls represent Cu, O, Cu vacancy and O vacancy, respectively.

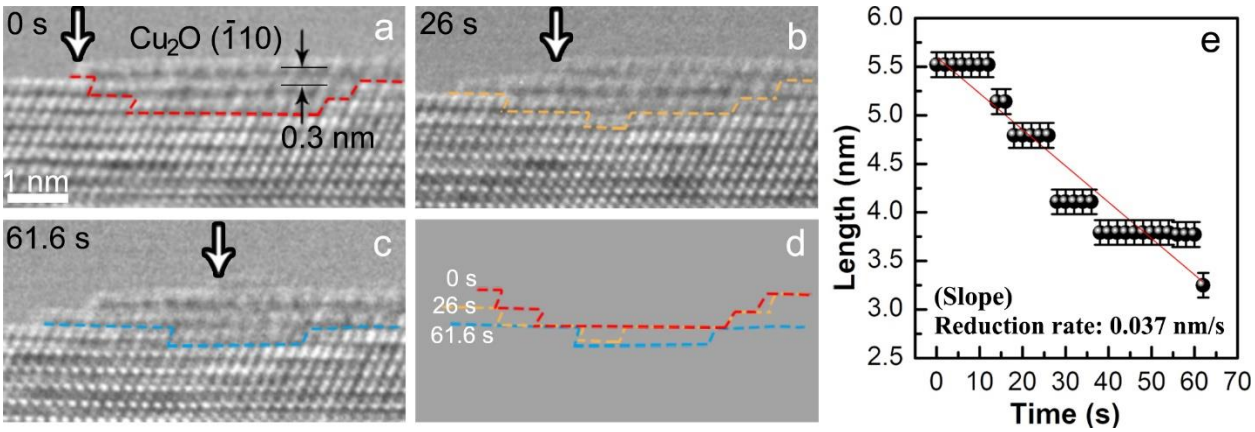

Figure S13. (a-c) In-situ TEM images showing the Cu_2O formation out of the CuO-superstructure (25% O vacancies during the continued H_2 gas exposure at T=300 °C and pH_2=0.5 Pa. The dashed lines mark the interface between the Cu_2O and the CuO-superstructure. The white arrows are used to track the decay motion of the outmost surface step. (d) Superimposed traces of the position and profile of the Cu_2O/CuO-superstructure interface at 0 s (red), 26 s (orange), and 61.6 s (blue), showing the inward migration of the interface toward the CuO-superstructure region. (e) The retraction motion distance of the outermost surface step (marked by the white arrows in (a-c)) as a function of the time, where the linear fitting (red line) yields a reduction rate (slope of the red line) of 0.037 nm/s, much slower than the decay rate (0.13 nm/s) of atomic steps on the CuO surface measured in Figs. 2g-i.

Supplementary Table 1

Energy barriers for migration of the O vacancy along pathways 1-4 (marked in Figure 4d) calculated using Perdew-Burke-Ernzerhof (PBE) functional and Heyd–Scuseria–Ernzerhof (HSE06) hybrid functional, respectively.

Pathway / Method	1	2	3	4
PBE	0.59 eV	0.57 eV	0.91 eV	1.1 eV
HSE06	0.61 eV	0.47 eV	0.91 eV	1.4 eV

References:

1. Sun, X. H.; Zhu, W. H.; Wu, D. X.; Liu, Z. Y.; Chen, X. B.; Yuan, L.; Wang, G.; Sharma, R.; Zhou, G. W., Atomic-scale mechanism of unidirectional oxide growth. *Adv. Funct. Mater.* **2020,** *30* (4), 1906504.

2. Sun, X. H.; Zhu, W. H.; Wu, D. X.; Li, C. R.; Wang, J. Y.; Zhu, Y. G.; Chen, X. B.; Boscoboinik, J. A.; Sharma, R.; Zhou, G. W., Surface-reaction induced structural oscillations in the subsurface. *Nat. Commun.* **2020,** *11* (1), 305.

3. Kresse, G.; Hafner, J., Ab initio molecular dynamics for liquid metals. *Phys. Rev. B* **1993,** *47* (1), 558.

4. Kresse, G.; Hafner, J., Ab initio molecular-dynamics simulation of the liquid-metal–amorphous-semiconductor transition in germanium. *Phys. Rev. B* **1994,** *49* (20), 14251.

5. Kresse, G.; Furthmüller, J., Efficiency of ab-initio total energy calculations for metals and semiconductors using a plane-wave basis set. *Comput. Mater. Sci.* **1996,** *6* (1), 15-50..

6. Perdew, J. P.; Burke, K.; Ernzerhof, M., Generalized gradient approximation made simple. *Phys. Rev. Lett.* **1996,** *77* (18), 3865.

7. Kresse, G.; Joubert, D., From ultrasoft pseudopotentials to the projector augmented-wave method. *Phys. Rev. B* **1999,** *59* (3), 1758.

8. Wang, L.; Maxisch, T.; Ceder, G., Oxidation energies of transition metal oxides within the GGA+ U framework. *Phys. Rev. B* **2006,** *73* (19), 195107.

9. Maimaiti, Y.; Nolan, M.; Elliott, S. D., Reduction mechanisms of the CuO (111) surface through surface oxygen vacancy formation and hydrogen adsorption. *Phys. Chem. Chem. Phys.* **2014,** *16* (7), 3036-3046.

10. Nolan, M.; Elliott, S. D., The p-type conduction mechanism in Cu_2O: a first principles study. *Phys. Chem. Chem. Phys.* **2006,** *8* (45), 5350-5358.

11. Chen, T.; Zhang, T.; Wang, G.; Zhou, J.; Zhang, J.; Liu, Y., Effect of CuO on the microstructure and electrical properties of $Ba_{0.85}Ca_{0.15}Ti_{0.90}Zr_{0.10}O_3$ piezoceramics. *J. Mater. Sci.* **2012,** 47 (11), 4612-4619.

12. Henkelman, G.; Uberuaga, B. P.; Jónsson, H., A climbing image nudged elastic band method for finding saddle points and minimum energy paths. *J. Chem. Phys.* **2000,** *113* (22), 9901-9904.

Atomic Origin of the Autocatalytic Reduction of Monoclinic CuO in a Hydrogen Atmosphere

Xianhu Sun[1†], Dongxiang Wu[1†], Wenhui Zhu[1], Xiaobo Chen[1], Renu Sharma[2], Judith C. Yang[3], Guangwen Zhou[1*]

[1.] Department of Mechanical Engineering & Materials Science and Engineering Program, State University of New York, Binghamton, New York 13902, United States

[2.] Nanoscale Device Characterization Division, National Institute of Standards and Technology, Gaithersburg, Maryland 20899, United States

[3.] Department of Chemical and Petroleum Engineering, University of Pittsburgh, Pittsburgh, Pennsylvania 15261, United States

† These authors contributed equally to the work

* Correspondence to: gzhou@binghamton.edu

ABSTRACT:

Reducibility is key for the use of bulk metal oxides in chemical transformations involving redox reactions, but probing microscopic processes of oxide reduction is challenging. This is because the insulating nature of bulk oxides restricts ion and electron spectroscopic measurements of oxide surfaces. Herein, using a combination of environmental transmission electron microscopy and atomistic modeling, we report direct in situ atomic-scale observations of the surface and subsurface dynamics and show that the hydrogen-induced CuO reduction occurs through the receding motion of Cu−O/Cu bilayer steps at the surface, the formation of the partially reduced CuO superstructure by the self-ordering of O vacancies in the subsurface, and the collapse of Cu-O layers in the bulk. All these substeps can be traced back to the progressively increased concentration and activity of O vacancies in the surface and subsurface of the oxide, thereby leading to the self-accelerated oxide reduction. These results demonstrate the microscopic details that may have a broader applicability in modulating various redox processes.

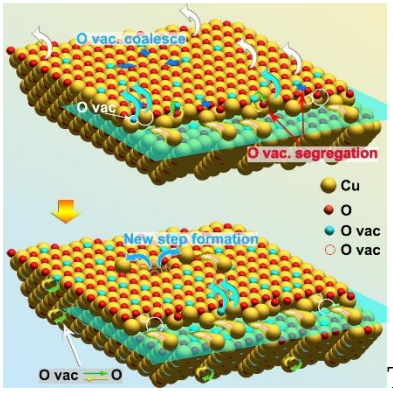

TOC Graphic

Redox reactions play a vital role in chemical transformation processes of materials including heterogeneous catalysis, battery cycling, and corrosion.[1-4] This is exemplified by the well-known Mars-van Krevelen (MvK) mechanism of catalytic oxidation over metal oxides, during which the reactants are oxidized by the redox cycle of the oxide catalyst.[5] That is, the catalyst itself is altered by the reaction it catalyzes. Namely, the reactants are oxidized into oxygenated compounds by the oxide catalyst, which is accompanied by the partial reduction of the oxide and its reoxidation back to the initial state by O_2. Therefore, the reducibility of the oxide is closely correlated with the catalytic activity for oxidation. It is generally assumed that the oxide in a higher oxidation state of the metal has the higher reducibility (and lower stability) than that of a lower oxidation state because the metal atom in the higher oxidation state is more electron-deficient and thus has a larger tendency to accept electrons.[6, 7] Thermodynamically, the oxide reduction should occur more rapidly at first and then slow as the driving force of the reaction diminishes. In contrast to this thermodynamic expectation, here we focus on the kinetic aspect and report the direct imaging and temporal evolution of CuO reduction and show an autocatalytic process in which the reduction rate of the bulk oxide increases progressively as the reaction proceeds. This process involves the generation of O vacancies at the oxide surface upon the formation of oxygenated products that desorb from the surface and the inward migration and accumulation of O vacancies in the subsurface region (with a depth of several nanometers away from the surface) of the oxide. This phenomenon cannot be revealed readily with the use of traditional surface science and bulk materials science tools because of their inability to unambiguously differentiate the surface and subsurface regions due to the spatiotemporal superposition of the detected signal originating from multiple atomic layers.[7-9]

In addition, the insulating nature of the oxides hampers the study of oxide surfaces because many surface-sensitive techniques are based on the detection of charged particles such as electrons and ions and cannot be applied to bulk oxides which are insulators or wide-band-gap semiconductors.[10, 11] One way to circumvent the charging effects is to oxidize a metallic surface by dosing it with a small amount of O_2 under ultrahigh vacuum (UHV) conditions, thereby producing an ultrathin oxide film (only a few atoms in thickness) on the conductive substrate.[9, 12] Such ultrathin oxide films can be considered "electrically conductive" counterparts of insulating bulk oxides, thereby allowing the use of surface science techniques to study the reduction of surface oxides.[9, 13] However, the ultrathin nature of the oxide film also makes it significantly different from the bulk counterpart, including the abrupt discontinuity and breaking of the translation symmetry along the thickness direction and interfacial strains. In particular, there is a lack of a genuine subsurface region within the ultrathin oxide film because of the atomic proximity between the oxide surface and oxide-metal interface. Therefore, the insight obtained from the ultrathin oxide overlayer may not represent the intrinsic behavior of the bulk oxide.

In contrast, transmission electron microscopy (TEM) is not subject to the aforementioned limitations of traditional surface science tools and offers a unique window to study the reduction of the oxide at an atomic scale from both the surface and subsurface regions at the same time.[14, 15] Particularly, the recent developments in environmental TEM have enabled us to dynamically observe a gas-surface reaction under a gas-controlled environment.[16] This was achieved by incorporating differential pumping local to the specimen, thereby allowing for the volume around the specimen to be filled with gases so that the pressure of the volume can be kept higher than that of the TEM column. By employing a dedicated environmental TEM equipped with an image corrector and a differential pumping system, herein we report an in situ atomic-scale study of the

reduction dynamics of CuO by flowing H_2 gas in the sample region while simultaneously monitoring the structure evolution from the outermost surface to deeper atomic layers under the reaction conditions. CuO was chosen as a model system because it is widely used as a support for metal catalysts, and as a catalyst on its own, in various catalytic oxidation reactions, including the water-gas-shift reaction,[17] methanol synthesis and oxidation,[7, 18] and the oxidative dehydrogenation of alcohols.[19] In these reactions, the Cu oxide is an active catalyst and hydrogen is involved either as a reactant or as a product. [1, 7, 8]

Our in situ TEM experiments involve two steps (detailed in the Supporting Information), starting with the in situ synthesis of CuO by exposing metallic Cu to O_2 gas at 400 ºC. This is followed by first cooling the oxidized sample to 300 °C in O_2 and then by switching to vacuum by pumping out the O_2 gas to the base pressure (1×10^{-5} Pa) of the E-TEM in the specimen region. The oxide reduction is performed by introducing a H_2 gas flow at 300 °C. Figure 1 a shows a high-resolution TEM (HRTEM) image of the CuO formed from the oxidation of Cu at an oxygen pressure (pO_2) of 0.53 Pa and a temperature (T) of 300 °C. The CuO surface shows a step-terrace morphology and is oriented along the $[\bar{1}10]$ direction and viewed along the $[\bar{1}\bar{1}\bar{1}]$ zone axis, as confirmed by the fast Fourier transform (FFT) diffractogram (inset) of the HRTEM image in Figure 1 a. Figure 1 b is a magnified HRTEM image of the area marked with the white dashed square in Figure 1 a, showing the perfect CuO lattice as alternately bright and significantly dim contrasts of atomic columns. Figure 1 c illustrates the atomic structure of the stoichiometric monoclinic CuO (space group $C\,2/c\,1$) consisting of the presence of Cu-O and pure Cu layers when viewed along the $[\bar{1}\bar{1}\bar{1}]$ zone axis. The red inset in Figure 1 b is a simulated HRTEM image of the stoichiometric CuO along the $[\bar{1}\bar{1}\bar{1}]$ zone axis (Figure S1). Based on the good match between the experimental and simulated HRTEM images along with the stoichiometric CuO

structure in Figure 1 c, we can identify that the atomic layers consisting of Cu-O atomic columns show the bright image contrast, whereas the atomic layers with the significantly dimmed image contrast correspond to pure Cu atomic columns. Our in situ TEM images indicate that the CuO lattice is relatively stable at 300 ℃ in vacuum and the continuous electron beam observations do not induce noticeable oxide reduction, as confirmed from the negligible changes in the lattice contrast and the step-terrace surface morphology (Figure S2 and Supplementary Movie S1).

H_2 gas is then introduced to the sample region and induces the oxide reduction. Figure 1 d shows an HRTEM snapshot of the same sample area after the exposure to a H_2 gas flow at hydrogen pressure (pH_2) of 0.5 Pa and T ≈ 300 ℃. The oxide transforms into a superlattice contrast, which is featured from the surface to the deeper atomic layers with a depth of ≈ 3 nm. This is also confirmed by the diffractogram (inset of Figure 1 d) in which the superlattice reflections are marked by white circles. Figure 1 e is an enlarged HRTEM view of the superlattice region as marked by the white dashed square in Figure 1 d. By comparing the HRTEM image of the perfect CuO lattice (Figure 1 b), the Cu-O planes transform into alternately bright and dim contrasts of atomic columns. This suggests the oxide-reduction-induced loss of lattice O, where the resultant O vacancies self-order into a superlattice structure by condensing onto every other $(\bar{2}02)$ planes of the CuO lattice and the image contrast for the O-deficient Cu-O columns becomes relatively dim. Figure 1 f is a structure model of the O-deficient CuO lattice with 50 % O vacancies in every other Cu-O column of the CuO lattice. The blue inset in Figure 1 e is a simulated HRTEM image based on the O-deficient CuO lattice in Figure 1 f (Figure S3). As indicated by the intensity profile analysis in Figure 1 e, the image intensity for the O-deficient Cu-O columns is about 30 % weaker than that for the intact Cu-O column, matching well with the experimental HRTEM image.

Therefore, the formed superlattice is O-deficient CuO in which 25% of the lattice oxygen sites in the stoichiometric CuO are vacant.

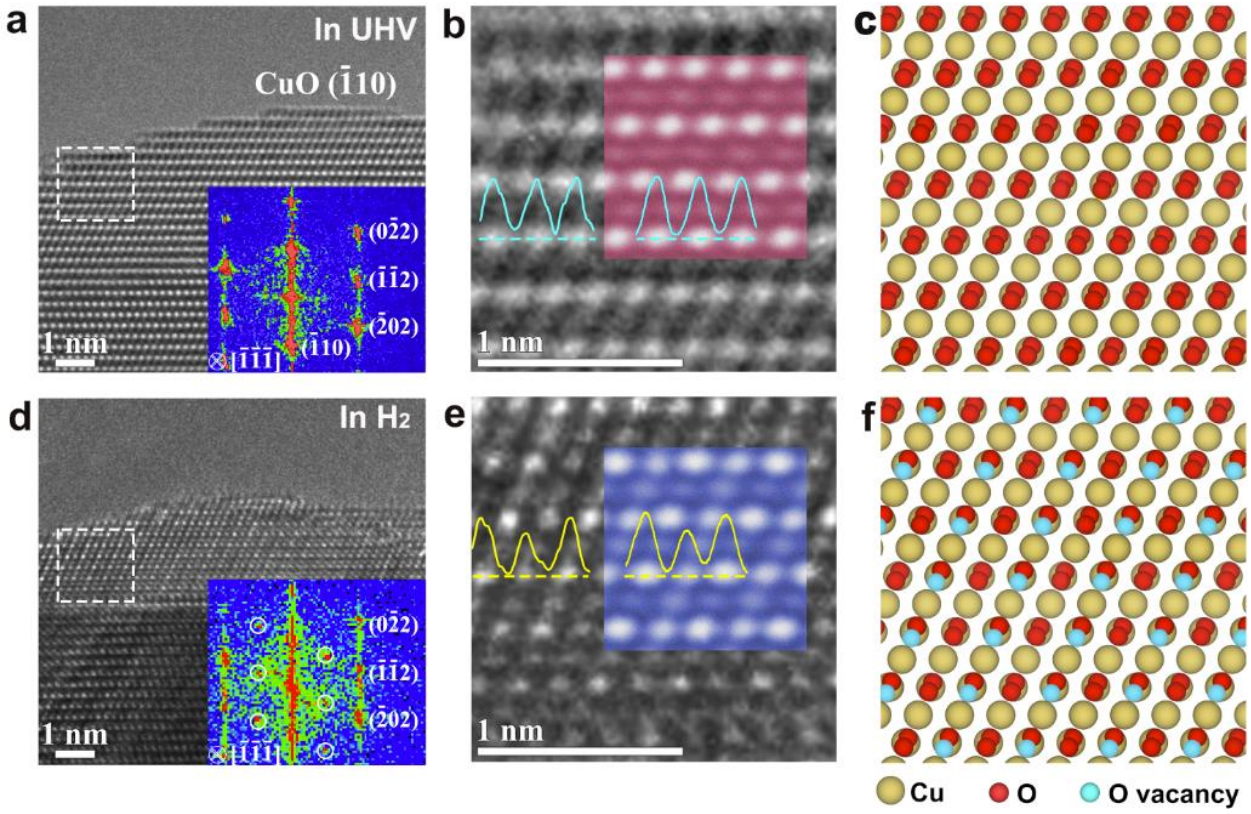

Figure 1. Subsurface oxygen vacancy ordering induced superlattice contrast. (a) HRTEM image of a stoichiometric CuO at 300 °C in a vacuum (Supplementary Movie S1), viewed along the $[\bar{1}\bar{1}\bar{1}]$ zone axis. Inset is a FFT diffractogram of the HRTEM image. (b) Magnified view of the region marked with the white dashed square in panel a. The red inset is a simulated HRTEM image based on (c) the stoichiometric CuO structure. (d) HRTEM image of the same sample area after the exposure to the H_2 gas flow at $pH_2 \approx 0.5$ Pa and T ≈ 300 °C. The inset is a FFT diffractogram of the HRTEM image showing the presence of superlattice diffraction spots (marked by white circles). (e) Magnified image from the white dashed square in panel d. The blue inset is a simulated HRTEM image based on (f) a CuO superstructure model consisting of 50 % O vacancies in every other Cu–O column (the positions of O vacancies are represented by cyan balls). The cyan and yellow lines in panels b and e are intensity profiles along the dashed lines.

Figure 2 illustrates a time sequence of HRTEM images (Supplementary Movie S2), showing the autocatalytic (accelerated) reduction behavior of CuO in flowing H_2 gas at $pH_2 \approx 0.5$ Pa and T ≈ 300 °C. The CuO $(\bar{1}10)$ surface initially exhibits a step-terrace configuration consisting

of $(\bar{1}10)$ terraces and bilayer atomic steps, as marked by the black dashed line in Figure 2 a. As schematically shown in the upper inset in Figure 2 a, the bilayer atomic steps are composed of an outer Cu-O layer and an inner pure Cu layer with the step height of $d_{\mathrm{CuO}(\bar{1}10)} \approx 0.28$ nm, where the Cu-O/Cu bilayer step configuration of the CuO lattice was determined from the HRTEM images and the corresponding HRTEM image simulations shown in Figure 1. The oxide reduction proceeds by the retraction motion of the Cu-O/Cu bilayer atomic steps along the $(\bar{1}10)$ surface, as marked by double white arrows in Figure 2 a, d, and g, leading to the simultaneous removal of the Cu-O and Cu layers from the surface. As a result, the oxide surface is constantly terminated by the Cu-O layer during the oxide reduction due to the retraction motion of the bilayer atomic steps.

Initially, the oxide reduction rate is slow, as revealed by the slow lateral motion of the surface steps. By monitoring the evolution of the surface profile as marked by the black and red dashed lines in Figure 2 a and b, the oxide reduction rate can be determined by measuring the lateral motion of the surface steps and the resulting oxide shrinkage as a function of time. As shown in Figure 2 c, the surface retraction motion speed of the atomic steps and the oxide projection area reduction rate were measured to be 0.03±0.005 nm•s^{-1} and 0.03±0.007 nm^2•s^{-1}, respectively, in the first ≈ 100 s of the H_2 exposure. Panels d and e of Figure 2 present the HRTEM snapshots after the continuous H_2 exposure for 400 and 480 s, respectively, showing a faster rate of the oxide reduction (Figure 2 f). The surface retraction speed of the atomic steps and the oxide reduction rate were measured to be 0.07±0.009 nm•s^{-1} and 0.05±0.006 nm^2•s^{-1}, respectively, between 400 and 520 s of the H_2 exposure. Panels g and h of Figure 2 show the HRTEM images corresponding to the time stamps of 2210 and 2290 s of the H_2 exposure, respectively, illustrating the nucleation of new Cu-O/Cu bilayer atomic steps (marked by the blue arrow) by surface pitting at the flattened

terrace and their lateral retraction motion. Meanwhile, the step flow speed becomes 0.13±0.01 nm•s^{-1}, which results in the increased oxide reduction rate of 0.07±0.005 nm^2•s^{-1} (Figure 2 i).

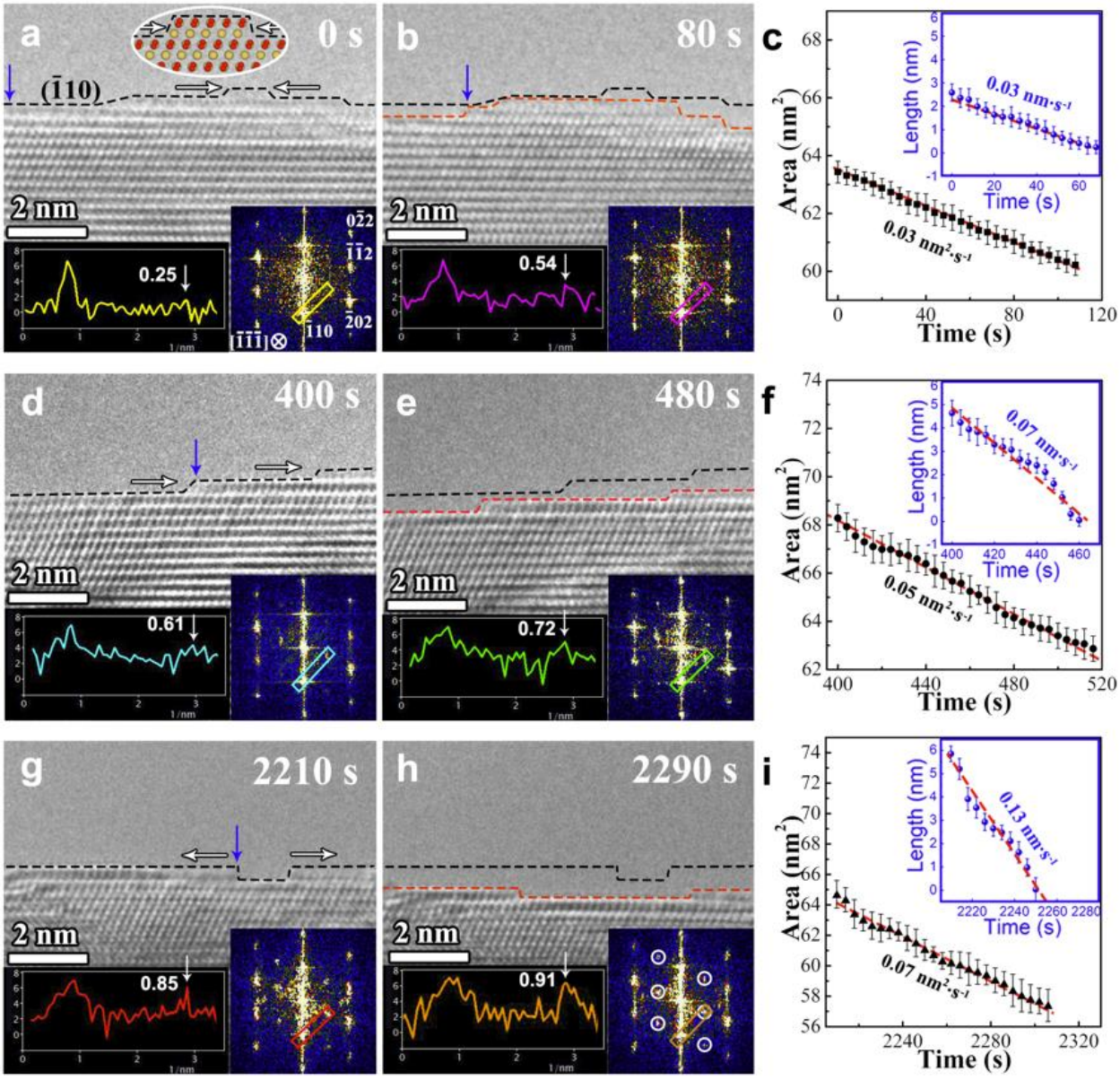

Figure 2. In situ atomic-scale imaging of the autocatalytic CuO reduction at $pH_2 \approx 0.5$ Pa and T ≈ 300 °C (Supplementary Movie S2). (a-c) HRTEM snapshots and the measured oxide reduction rate in the first ≈ 100 s of the H_2 exposure. The upper inset in panel a illustrates schematically the atomic configuration of the Cu-O/Cu bilayer surface step. The oxide surface is constantly terminated by the Cu-O plane by the retraction of Cu-O/Cu bilayer steps. (d-f) HRTEM images and the corresponding oxide reduction rate measured between ≈ 400 and 520 s of the H_2 exposure. (g-i) HRTEM snapshots and the oxide reduction rate measured between ≈ 2200 and 2310 s of the H_2 exposure. The insets in panels c, f, and i show the measured lateral motion speed of the bilayer atomic steps marked by blue arrows. The bottom-right insets in panels a, b, d, e, g, and h are the FFT diffractograms of the HRTEM images, where the superlattice

reflections are marked by the white circles. The bottom-left insets show the normalized intensity profiles and the intensity ratio of the superlattice spot with regard to the fundamental $(\bar{1}10)$ spot, where the two reflections are marked by the rectangle in the diffractograms. The error bars represent standard deviation uncertainties based on multiple measurements.

Fast Fourier transform diffractograms were also obtained from the HRTEM images shown in Figure 2 to illustrate the evolution of the crystal lattice over the continued exposure to the H_2 gas flow. The initially uniform lattice contrast gradually transforms to the superlattice contrast in the subsurface region. As shown in the FFT diffractograms (bottom-right insets of the HRTEM images in Figure 2) that were derived from entire HRTEM images, the presence of the superlattice reflections and their intensities becomes gradually more pronounced upon the continued H_2 exposure. This is evidenced by the normalized intensity profiles given in the bottom-left insets of the HRTEM images in Figure 2 and the measured intensity ratio of the superlattice reflection with respect to the fundamental $(\bar{1}10)$ spot. The increased intensity of the superlattice spots indicates the more pronounced ordering of O vacancies in the subsurface of the CuO with the continued H_2 exposure.[20]

Such accelerated oxide reduction kinetics, where were measured by monitoring the retraction motion of Cu-O/Cu bilayer atomic steps are observed from multiple samples. Figure 3 shows another example of the in-situ TEM observations of the CuO reduction. The oxide surface is relatively flat with the presence of a Cu-O/Cu bilayer atomic step on the right corner that soon moves out of the field of view via the retraction motion toward the right side (marked by the yellow arrow in Figure 3 a). As can be seen clearly in Figure 3 b, the surface area in the right corner (marked by the red arrow) develops into weakened image contrast as the reduction continues. This suggests that the oxide is gradually reduced in the local area, which eventually results in the formation of a surface pit with a depth of 0.28 nm (marked by the red arrows in Figure 3 c), that

442 is equivalent to the interplanar $(\bar{1}10)$ spacing of the CuO lattice and corresponds to the Cu-O and
443 Cu bilayers. The newly formed steps associated with the surface pit then undergo the retraction
444 motion along the surface in the opposite directions (marked by the red arrow in Figure 3 d), leading
445 to the widening of the exposed Cu-O surface by the gradual removal of the existing Cu-O/Cu
446 bilayers from the surface. This process of nucleating new bilayer atomic steps by the localized
447 oxide reduction (as marked by the blue arrows in Figure 3 e) and the lateral propagation of the
448 newly formed steps repeats itself during the oxide reduction, resulting in the area shrinkage of the
449 oxide. It is worth noting here that the field of view was under uniform illumination of the electron
450 beam (e-beam) and the oxide would be reduced homogeneously across the area if there was e-
451 beam induced oxide reduction. The negligible e-beam effect on the oxide reduction was further
452 confirmed by blanking the e-beam during the H_2 exposure. Figure 3 g and h shows two HRTEM
453 snapshots between which the e-beam was blanked for $\approx$ 60 s and then unblanked for TEM imaging.
454 As shown by the surface profiles given in Figure 3 g and h, the oxide still undergoes the reduction
455 in the dark by the removal of up to two Cu-O/Cu bilayers. Figure 3 i shows the autocatalytic
456 (accelerated) shrinkage of the oxide as a function of the H_2 exposure time, as indicated by the
457 increasingly steeper slope of the plot irrespective of the unblanking or blanking the e-beam.
458 Consistent with the observation in Figure 2, the subsurface region of the oxide gradually develops
459 into the superlattice image contrast. This is evident from the corresponding FFT diffractograms of
460 the entire HRTEM images, showing that the superlattice reflection spots are absent in the
461 beginning of the H_2 exposure (Figure 3 a), then gradually become visible (Figure 3 e) and
462 increasingly more pronounced (Figure 3 h) upon the continued H_2 exposure. It is worth mentioning
463 that the measured oxide reduction rates in Figures 2 and 3 are based on the surface decay of atomic
464 layers rather than the measurement of the shrinkage of the projection area of the total oxide.

Therefore, any volume shrinkages induced by O vacancies in the oxide do not affect our measurements. Meanwhile, our in situ HRTEM imaging shows that the partially reduced CuO superlattice (with 25% O vacancies) and the parent CuO have a coherent interface (Figure S4), indicating that the vacancy-induced volume shrinkage is negligible.

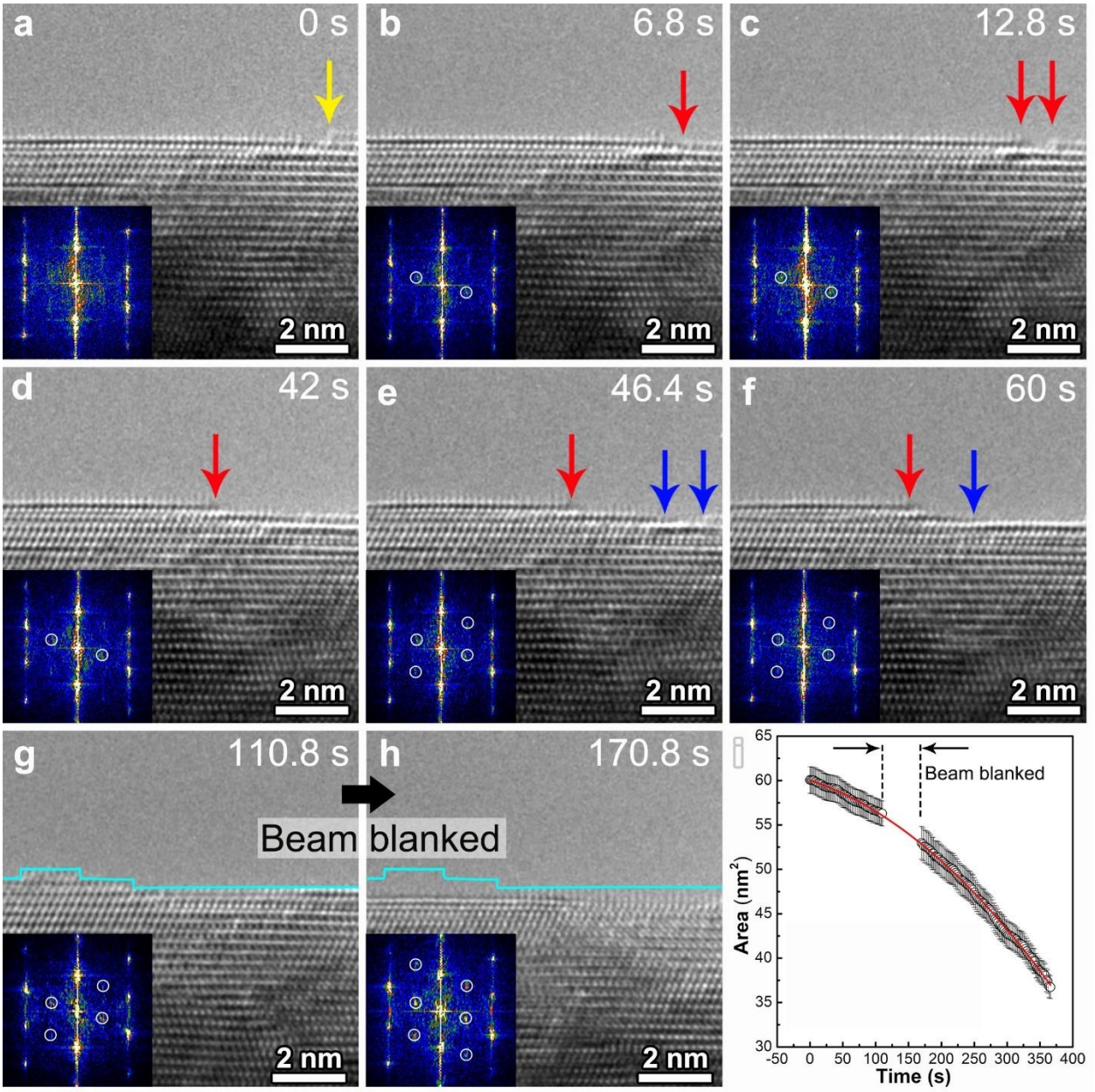

Figure 3. In situ TEM imaging of the surface retraction of atomic steps and the gradual development of the superlattice contrast in the subsurface during the CuO reduction at T=300 °C and pH_2=0.5 Pa. (a-h) Time-sequence HRTEM images (Supplementary Movie S3) showing the surface retraction motion of Cu-O/Cu

bilayer atomic steps and the formation of new Cu-O/Cu steps via surface pitting at the terrace. Between panel g and panel h, the e-beam was blanked for ≈ 60 s to examine possible electron beam irradiation effects on the oxide reduction and then unblanked for TEM imaging. Insets in panels a-h are FFT diffractograms of the HRTEM images showing that the superlattice reflections (as marked by white circles) become increasingly pronounced upon the continued H_2 exposure. (i) The retraction rate of the oxide surface is measured from the in situ TEM movie, where the progressively increased slope indicates the autocatalytic oxide reduction. The error bars represent standard deviation uncertainties based on multiple measurements, and the steeper slope of the plot at the later stage results in more overlapping of the error bars along the vertical direction.

The above in situ TEM observations (in the cross-sectional view) show that the oxide reduction occurs via the retraction motion of Cu-O/Cu bilayer atomic steps. The similar oxide-reduction-induced retraction motion of surface steps also occurs on the planar surfaces, as observed from the in situ TEM imaging in the plan view (Figures S5 and S6). This suggests that surface steps are effective for H adsorption, thereby promoting step-edge detachment via the reaction between adsorbed H and lattice O at the step edge. This was confirmed using density-functional theory (DFT) by examining the adsorption energies of H at different surface sites, which are found to be -2.04 and -1.77 eV for the step edge and the terrace region, respectively (Figure S7). Although step edges are more favorable for H adsorption, their relative contribution to the overall reduction kinetics also depends on the area fraction. Because the area fraction of the surface terraces is much larger than that for the surface steps, the contribution from H adsorption on the terraces is significant. The reaction between adsorbed H and lattice O at terraces and along surface steps results in the formation of H_2O molecules that easily desorb from the surface due to the high reaction temperature, leaving behind O vacancies. The reaction of adsorbed H with lattice O at the terraces is evidenced by the observed formation of new Cu-O/Cu bilayer steps on flat terraces (Figure 2 g and Figure 3 c), where the surface aggregation of O vacancies results in a localized higher concentration of O vacancies, thereby destabilizing the oxide and resulting in the formation

of surface pits. On the other hand, O vacancies generated in terrace areas adjacent to surface steps can segregate toward surface steps and thus make the Cu atoms at the step edge further under-coordinated, thereby promoting the retraction motion of surface steps by the step-edge detachment as described later by DFT results. The migration of surface Cu atoms (freed from the oxide reduction) into the bulk is unlikely. This is because the CuO lattice, particularly the partially reduced CuO superstructure (with 25% O vacancies), is dominated by O vacancies, whereas the Cu sublattice is intact (Figure S4). Instead, the Cu atoms released from the retraction motion of surface steps and the formation of surface pits aggregate on the inner surface region of the oxide and form a Cu overlayer, as shown by the presence of the Moiré fringe contrast (Figure S8). In addition, O vacancies produced via the H_2O formation at the terraces can also migrate into the subsurface because of the counter diffusion of lattice O from the subsurface to the surface, thus sustaining the reduction reaction. The accumulation of O vacancies in the subsurface is evidenced by their progressive self-ordering into the CuO-superlattice, as revealed by the HRTEM images and diffractograms in Figures 1-3. The continued generation of O vacancies at the surface, including terraces and step edges, and their subsequent population along the surface steps and in the subsurface region increasingly destabilize the oxide and accelerate the oxide reduction. This is attributed to the atomic origin of the autocatalytic oxide reduction behavior.

Our in situ TEM observations show that the retraction motion of the surface steps occurs prior to the development of the superlattice in the subsurface. This indicates that the surface (particularly, the step edges) is the first place for O vacancy formation from the reaction between lattice O and adsorbed H, forming H_2O molecules that desorb from the surface. Oxygen vacancies generated near surface steps segregate to the surface step edge via surface diffusion, thereby leading to the Cu step edge detachment (and thus the step edge decay). The CuO superlattice

formation in the subsurface requires the population of O vacancies in the subsurface region, which may encounter a larger energy barrier for the migration of O vacancies from the surface into the subsurface than that for surface migration of the O vacancies. Therefore, the surface decay of atomic steps is kinetically more favorable than CuO superlattice formation in the subsurface.

This oxide reduction process was further elucidated by DFT modeling. Figure 4 a shows the DFT-obtained reaction pathway coordinate leading to the retraction motion of the surface step along the CuO($\bar{1}10$) surface. As marked in Figure 4 a, there are two kinds of crystallographically nonequivalent O sites (O-1 and O-2) at the step edge for the H-induced loss of the lattice O. By evaluating their vacancy formation energies, it was found that the O atom at the O-1 site is less stable and has a smaller vacancy formation energy of 0.71 eV than that of the O-2 site, which has the vacancy formation energy of 1.35 eV. Upon the O loss at the O-1 site (stage I), its adjacent Cu in the topmost Cu-O layer spontaneously detaches from the step edge (stage II), as indicated by the decrease in the system energy from 0.71 to 0.48 eV. The departure of the step-edge Cu atom reduces the coordination number of the O atom at the O-2 site from 3 to 2, which results in a lower O vacancy formation energy of 0.5 eV at the O-2 site (stage III). Upon the O loss from the O-1 site, the adjacent Cu in the second layer of the step edge becomes unstable and undergoes spontaneous step-edge detachment as indicated by the drop of the system energy to 0.01 eV, which is nearly the same as that in the initial state (stage IV in Figure 4 a). This process of the sequential loss of lattice O at the O-1 and O-2 sites and the resultant spontaneous step-edge detachment of the adjacent Cu atoms repeats itself, leading to the observed retraction motion of the Cu-O/Cu bilayer surface step that was experimentally observed in Figures 2 and 3.

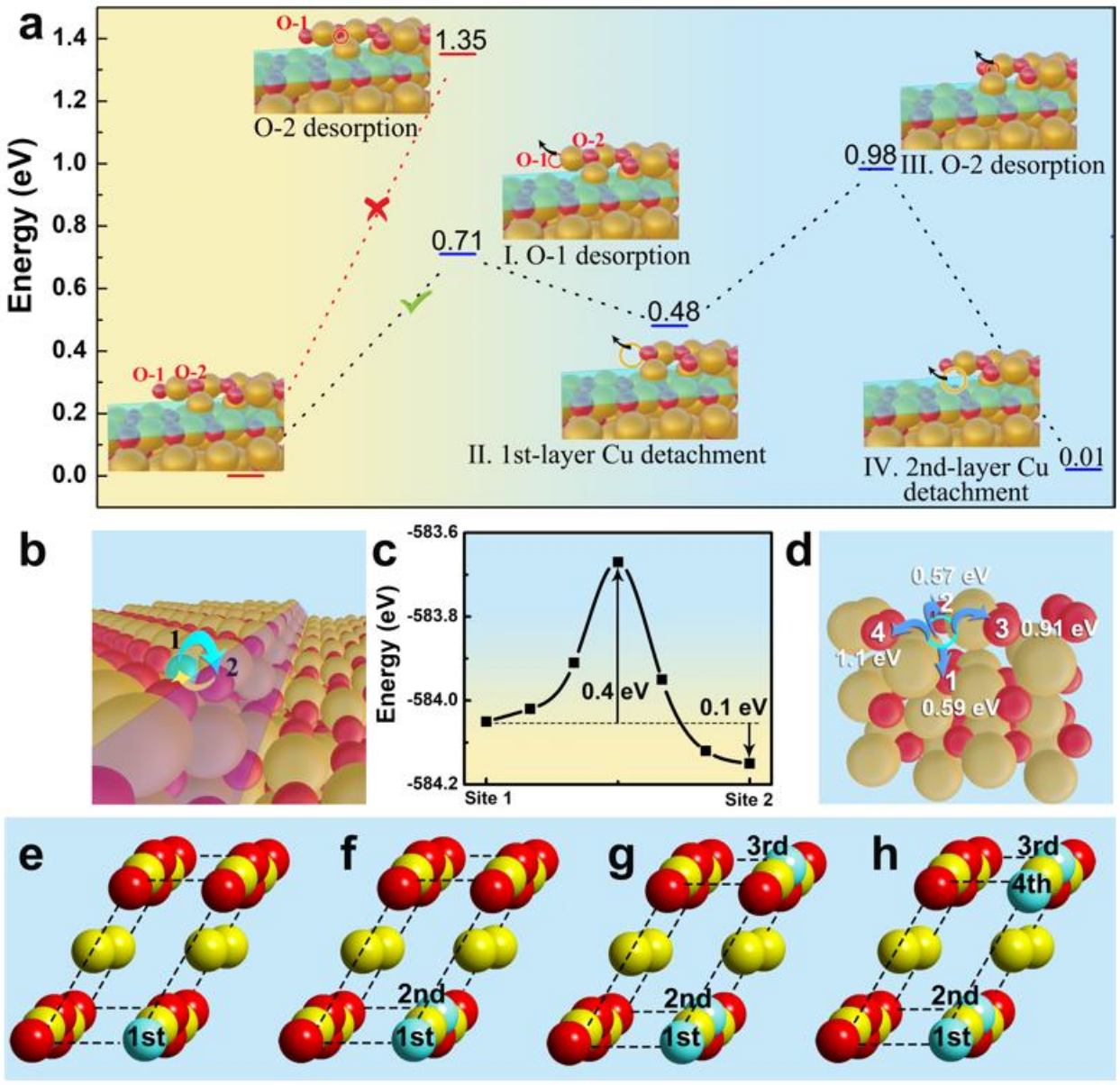

Figure 4. Atomic models of surface step retraction and O vacancy transport dynamics. (a) Reaction coordinate diagram of surface step retraction of CuO with reduction. (b) Schematic of the O vacancy (cyan ball) segregation to site 2 from site 1. (c) Energetic evaluation of the O vacancy segregation from site 1 to 2 in panel b. (d) Mass transport pathways of the newly formed O vacancy (cyan circle) on the surface. (e-h) Atomic models showing the sequence of lattice O desorption in CuO at favorable sites, where the resultant O vacancies are marked by cyan balls. Yellow, red, and cyan balls represent Cu and O atoms and O vacancies, respectively.

In addition, when the O vacancies are produced in the terrace area adjacent to the surface step, they tend to segregate to the step edge and therefore further promote the Cu step edge

detachment. This is shown in Figure 4 b, where sites 1 and 2 represent an O vacancy (light blue ball) and an adjacent lattice O at the step edge, respectively. Figure 4 c illustrates the DFT-obtained reaction pathway coordinate, showing that the segregation of the O vacancy to the lattice O site at the step edge lowers the system energy by 0.1 eV with a diffusion barrier of 0.4 eV. One important message from the above DFT modeling is that the H adsorption-induced O loss at the step edges and in their adjacent terrace destabilizes Cu atoms within the step edge, thereby leading to the Cu step edge detachment and the collapse of the oxide lattice along the step edge. This process leads to the annihilation of O vacancies and is in contrast to H adsorption in terrace areas that are relatively far away from the surface steps, where the terrace vacancies can coalesce into surface pits or diffuse into the subsurface region.

Our DFT results further elucidate that when one H_2 molecule is placed on the top of surface O, the H_2 molecule dissociates spontaneously into two H atoms that bond with the adjacent lattice O to form two hydroxyls (Figure S9), which is in agreement with other DFT computations.[21] The continued H adsorption gives rise to the formation of more OH species that remain stable at the surface until a surface coverage of 0.625 monolayer (ML) is reached, beyond which the further H adsorption leads to the formation of H_2O molecules that desorb spontaneously from the surface (Figure S10). The H_2O desorption results in the loss of the lattice O with the concomitant formation of O vacancies at the oxide surface. As shown in Figure 4 d and Supplementary Table 1, the formed O vacancy (cyan open circle) has two possible migration pathways: (i) diffusion in the surface layer along the site 2 direction with a diffusion barrier of 0.57 eV and (ii) migration into the subsurface along the site 1 direction with a diffusion barrier of 0.59 eV. The small barrier for the subsurface migration suggests that the O vacancies formed at the surface upon H_2O desorption can readily populate in the subsurface region and self-order into the superlattice structure, as seen from

Figures 1-3. The O vacancy diffusion pathways along the site 3 and site 4 directions (or the counterpart diffusion of the lattice O) in Figure 4 d can be ruled out due to the high energy barriers of 0.91 and 1.1 eV, respectively, to cross the Cu-Cu bridge sites. DFT calculations were also used to model the self-ordering process of O vacancies in the subsurface by evaluating the O vacancy formation energies at various sites of the CuO lattice. Figure 4e-h shows the energetically most favorable pathway for the sequential formation of four O vacancies with energy penalties of 2.5, 1.4, 1.4, and 0.4 eV, respectively. As shown by HRTEM image and diffraction simulations in Figures 1 and S11, the resulting O-deficient CuO lattice (Figure 4 h) contains 25 % O vacancies and reproduces the experimentally observed superlattice contrast and FFT diffractogram. These DFT results substantiate the self-ordering process of the O vacancies in Figure 4 e- h and confirm the experimentally observed evolution of the CuO-superlattice structure shown in Figures 1-3. The CuO is partially reduced to the superlattice structure because of the deficiency of O in the lattice.

It has been reported by Tu et al.[22] that the diffusion barrier for O migration in CuO is inversely proportional to the concentration of O vacancies, that is, the greater the concentration, the lower the diffusion barrier. Thus, the self-ordering of O vacancies is promoted upon the progressive accumulation of O vacancies in the subsurface region. This is in agreement with the in situ HRTEM observations (Figures 2 and 3), which show that the superlattice contrast in the subsurface region becomes increasingly pronounced with continued H_2 exposure. The continued accumulation of O vacancies makes the Cu atoms increasingly under-coordinated and destabilizes the oxide. This is evidenced by the formation of surface pits with a depth of 0.28 nm (equivalent to the thickness of the Cu-O/Cu bilayer), where the tendency for surface O vacancies to cluster in the terrace (Figure S12) results in a locally higher concentration of O vacancies and thus drives the collapse of the CuO lattice in the surface layer (Figures 2 g, and 3 c, and e). The collapse gives

602 rise to the concomitant formation of new Cu-O/Cu bilayer steps at the terraces and further speeds
603 up the oxide reduction evidenced by the retraction motion of the surface steps.

604 The accumulated O vacancies in the subsurface self-order into the CuO-superlattice with a
605 25% vacancy concentration (Figure 1 f and Figure 4 h), as confirmed from our in situ HRTEM
606 observations taken from on multiple samples (Figures 1-3). The further accumulation of O
607 vacancies with higher vacancy concentrations than that in the CuO superlattice can drive the
608 collapse of the oxide lattice in the bulk, as evidenced by in situ TEM images shown in Figure 5
609 (Supplementary Movie S4). Figure 5 a-c illustrates HRTEM snapshots from the movie showing
610 the lateral growth of a stacking fault induced by the collapse of the Cu-O layer in the subsurface
611 region that is $\approx$ 3 nm away from the outermost surface. In the first 34 s, the stacking fault
612 propagates laterally by 1.5 nm from the orange arrow (Figure 5 a) to the position of the cyan arrow
613 (Figure 5 b) and then by another 2.2 nm to the position of the red arrow after 51 s (Figure 5 c). The
614 bottom-right insets in Figure 5 a-b are the magnified HRTEM view of the regions marked by the
615 white dashed squares, showing the partial missing of the atomic plane in the growth front of the
616 stacking fault. Structurally, the CuO lattice consists of sequentially stacked Cu-O/Cu layers, as
617 labeled by labels of "A", "B", "C", and "D" in Figure 5 d. The "C" layer is partially missing on
618 the right side, leading to the formation of an edge dislocation-like feature indicated by a red "T"
619 in the stacking fault area in Figure 5 d and schematically shown in Figure 5 e.

620 This partially missing atomic plane corresponds to the collapse of the Cu-O layer because
621 the pure Cu layers in the CuO lattice are barely visible in the HRTEM images (Figure 1). The
622 collapse of the Cu-O layer (i.e., the C layer marked in Figure 5d) can be attributed to the
623 accumulation of O vacancies in the atomic plane, making the Cu atoms in the Cu-O layer
624 significantly under-coordinated. Cu oxides (Cu_2O and CuO) formed from the oxidation of Cu are

intrinsically Cu-deficient because of the existence of a low concentration (1.2%) of Cu vacancies,[23-24] where the oxide growth is controlled by the outward Cu vacancy-assisted diffusion of Cu atoms from the Cu substrate through the Cu oxides toward the CuO surface.[16, 23, 25] As a result of the overpopulation of O vacancies in the Cu-O plane, the Cu sublattice in the local region becomes unstable, and Cu atoms in the Cu-O plane diffuse away to native Cu vacant sites in neighboring planes of the CuO lattice. DFT calculations were also employed to confirm the tendency for the departure of the Cu atoms in the "C" layer leading to the stacking fault growth driven by the accumulation of O vacancies. As shown in Figure 5 e, we first desorb the O from the Cu-O column at site 1 in front of the stacking fault (which results in a pure Cu atom column), and move the Cu atom at site 1 to the Cu vacancies at site 2 and then to site 3. By evaluating the system energies by placing the Cu atom at the different Cu vacant sites, our DFT results (Figure 5 f) show that the migration of the Cu atom from the stacking fault front (site 1) to site 2 and then to site 3 in the adjacent layers is a spontaneous process of lowering the system energy. This confirms the stacking fault growth by the condensation of O vacancies into the Cu-O layers of the CuO lattice, which further speeds up the oxide reduction in the bulk.

In addition to the stacking fault formation, we also observed Cu_2O formation by following the transformation pathway of CuO→CuO superstructure (25% O vacancies)→Cu_2O during the continued H_2 exposure (Figure S13). Consistent with the thermodynamic expectation, our in-situ TEM imaging also confirms that Cu_2O is more resistant to reduction than CuO under the same reaction conditions of H_2 pressure and temperature. That is, the autocatalytic CuO reduction terminates after the formation of Cu_2O, which shows a slower reduction rate. The oxide reduction-induced phase transformation is also tied to a decrease in the oxidation state of Cu. The dissociative H_2 adsorption by lattice O^{2-} results in the formation of OH^-. To maintain the charge balance, the

neighboring Cu cation is reduced from the +2 state to the +1 state. The Cu^{1+} can be further reduced to metallic Cu after the OH combines with another H to form H_2O. This is consistent with the experimentally observed receding motion of the atomic steps (Figures 2 and 3) and the Cu overlayer formation (Figure S8). Alternatively, if the H_2O formation is relatively slower than the fast dissociative H_2 adsorption, Cu^{1+} is overpopulated, resulting in Cu_2O formation by following the transformation pathway of CuO→CuO superstructure (25% O vacancies)→Cu_2O during the continued H_2 exposure as also shown from our in situ TEM observations (Figure S13).

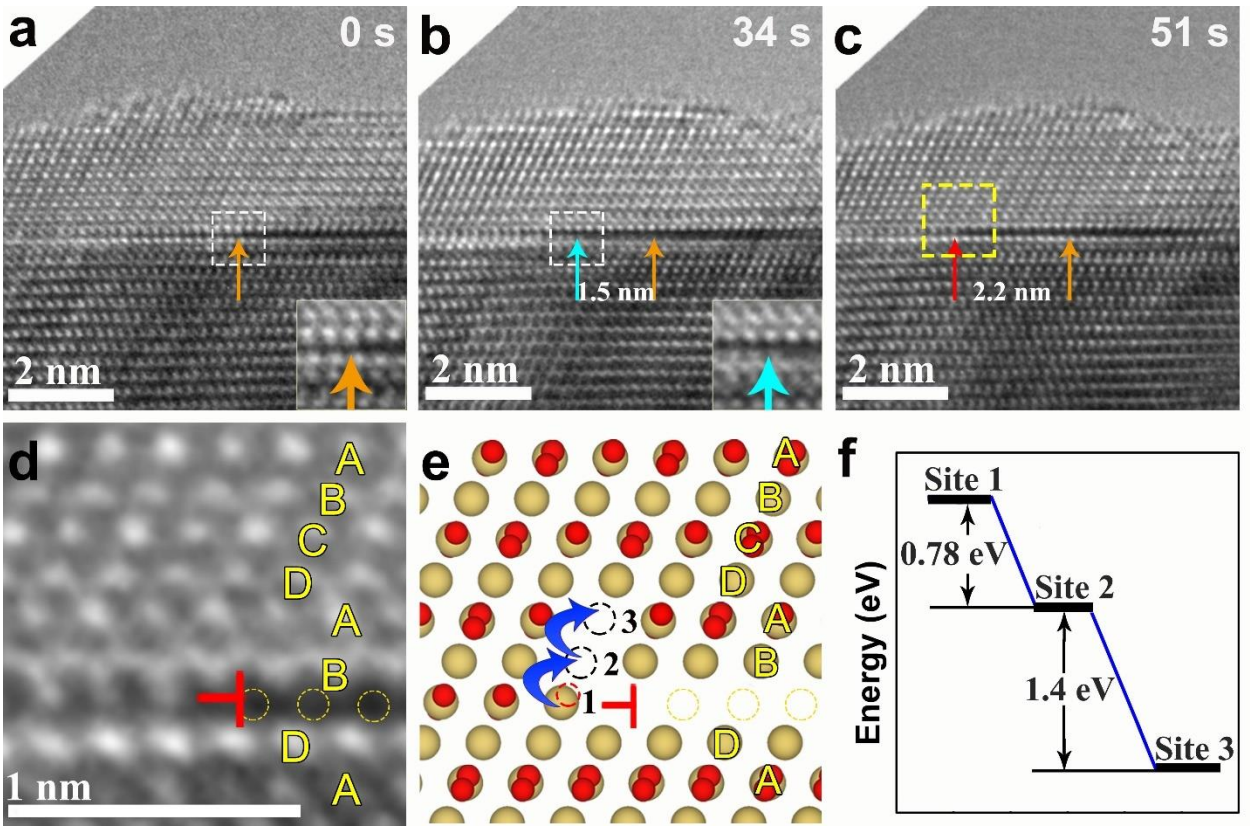

Figure 5. Stacking fault propagation resulting from O vacancy accumulation in the bulk. (a-c) Time-resolved HRTEM images (Supplementary Movie S4) of the CuO at $pH_2 \approx 0.5$ Pa and T ≈ 300 °C, showing that a stacking fault in the bulk propagates laterally toward the left. The orange, cyan, and red arrows mark the growth front of the stacking fault. The insets in panels a and b are enlarged views of the propagation front marked by the white dashed squares. (d) Enlarged HRTEM image of the front region of the stacking fault marked by the yellow dashed square in panel c, showing an edge dislocation for the partial absence of the "C-layer" of Cu-O atomic columns on the right side. (e) Atomic model of the stacking fault and migration of Cu atom from site 1 to site 2 and then to site 3, leading to propagation of the stacking fault

upon the aggregation of the O vacancies in the Cu-O plane. (f) DFT-computed free energies for the systems with the Cu atom placed at sites 1, 2, and 3 shown in panel e, respectively. Yellow balls, red balls, and yellow open circles represent Cu and O atoms and O vacancies, respectively.

As revealed from the above *in situ* TEM observations and DFT calculations, we show that the CuO reduction is induced by the loss of lattice O. Upon the reaction with adsorbed hydrogen, lattice O desorbs from both the terrace and the step edges in the form of H_2O molecules. H adsorption-induced O loss from the step edge destabilizes Cu atoms within the step edge, resulting in the oxide decay along the Cu-O/Cu bilayer step via the step edge detachment of Cu atoms. For the O loss in the terrace region adjacent to the step edge, the resultant O vacancies preferentially segregate to the step edge, facilitating the step edge detachment of Cu atoms. The oxide surface is constantly terminated by the Cu-O layer due to the retraction motion of the Cu-O/Cu bilayer atomic steps. For the O loss in terrace regions that are far away from the step edge, the resultant O vacancies have two migration pathways: i) aggregating into clusters of vacancies via surface diffusion, resulting in surface pitting and the concomitant formation of new surface steps and thereby further promoting the oxide reduction by the retraction motion of the step edges, and (ii) diffusing to the subsurface region and self-ordering into the CuO-superlattice. The further accumulation of O vacancies in the subsurface results in the collapse of the Cu-O layers, leading to the formation and propagation of stacking faults in the oxide lattice.

These results demonstrate the rich surface dynamics and the close coupling between the surface and subsurface during the oxide reduction process, underlining their importance in influencing the reaction kinetics. Clearly revealing such microscopic processes and decoupling surface and subsurface dynamics during the oxide reduction are experimentally challenging but indispensable for obtaining controllable functionalities of the oxides. This is because the chemical

and physical properties of metal oxides are crucially influenced by their stoichiometry, phase, microstructure, atomic termination, defects, and atomic coordination, all of which can be modified by a choice of the reduction treatment. Compared to a previous report showing the reduction pathway of $CuO \rightarrow Cu_2O \rightarrow Cu$,[7, 8] our work provides a more in-depth understanding with substeps of the oxide reduction involving the surface decay of Cu-O/Cu bilayer atomic steps, the formation of a partially reduced CuO superstructure via the self-ordering of O vacancies in the subsurface, and the collapse of Cu-O layers in the bulk for the further accumulation of O vacancies beyond the CuO superstructure. All these substeps leading to the accelerated oxide reduction can be traced back to the progressive loss of lattice O from the oxide surface, which results in the progressively increased concentration and activity of O vacancies in the surface and subsurface of the oxide.

In conclusion, we have identified the atomic-scale processes that lead to the autocatalytic reduction of bulk CuO. The reaction between adsorbed H and lattice O induces the loss of lattice O across the oxide surface, which in turn results in the generation of O vacancies at terraces and along surface steps. The oxide reduction occurs via the retraction motion of Cu-O/Cu bilayer atomic steps as a result of the O vacancy segregation toward existing surface steps and the formation of new surface steps by the O vacancy-aggregation-induced surface pitting. The oxide surface is constantly terminated by the Cu-O layer because of the decay motion of the Cu-O/Cu steps during the oxide reduction. Meanwhile, O vacancies produced at the surface terraces can also migrate into the subsurface and undergo self-ordering, forming a partially reduced CuO-superlattice structure. As reduction continues, O vacancies accumulate in the surface and subsurface region of the oxide, in turn speeding up the oxide reduction rate via the accelerated retraction motion of surface steps and the collapse of lattice planes in the bulk. The in situ

observations demonstrate the lively surface dynamics and the close coupling between the surface and subsurface during the oxide reduction process.

Supporting Information

Supporting Information is available free of charge at https://

Sample preparation, in situ TEM experimental procedures, HRTEM and diffractogram simulation details, and DFT calculation methods (PDF)

In situ TEM video illustrating that the CuO does not show noticeable surface decay at T=300 ℃ in ultra-high vacuum. (Movie S1)

In situ TEM video showing the autocatalytic CuO reduction at 0.53 Pa of H_2 gas flow and 300 ℃. The e-beam was blanked intermittently to mitigate electron beam irradiation effects on the reduction kinetics and then unblanked for TEM imaging. (Movie S2)

In situ TEM video showing the autocatalytic CuO reduction at 0.53 Pa of H_2 gas flow and 300 ℃. The e-beam was blanked for 60 s to examine any possible electron beam irradiation effects on the reduction kinetics and then unblanked for TEM imaging. (Movie S3)

In situ TEM imaging of the propagation of a stacking fault in the subsurface region of the CuO at 0.53 Pa of H_2 gas flow and 300 ℃. (Movie S4)

Acknowledgement: This work was supported by the U.S. Department of Energy, Office of Basic Energy Sciences, Division of Materials Sciences and Engineering under award no. DE-SC0001135. This research used resources of the Center for Functional Nanomaterials and the Scientific Data

and Computing Center, a component of the Computational Science Initiative, at Brookhaven National Laboratory, which is supported by the US Department of Energy, Office of Basic Energy Sciences, under contract no. DE-SC0012704. This work also used the computational resources from the Extreme Science and Engineering Discovery Environment (XSEDE) through allocation TG-DMR110009, which is supported by National Science Foundation Grant OCI-1053575.

Competing financial interests: The authors declare no competing financial interest.

References:

1. Kung, H. H. *Transition Metal Oxides: Surface Chemistry and Catalysis*; Elsevier: Amsterdam, The Netherlands, 1989.

2. Cao, J.; Rinaldi, A.; Plodinec, M.; Huang, X.; Willinger, E.; Hammud, A.; Hieke, S.; Beeg, S.; Gregoratti, L.; Colbea, C.; Schlogl, R.; Antonietti, M.; Greiner, M.; Willinger, M. In situ observation of oscillatory redox dynamics of copper. *Nat. Commun.* **2020,** *11* (1), 3554.

3. Wang, D.; He, H.; Han, L.; Lin, R.; Wang, J.; Wu, Z.; Liu, H.; Xin, H. L. Three-dimensional hollow-structured binary oxide particles as an advanced anode material for high-rate and long cycle life lithium-ion batteries. *Nano Energy* **2016,** *20*, 212-220.

4. Ruiz Puigdollers, A.; Schlexer, P.; Tosoni, S.; Pacchioni, G. Increasing oxide reducibility: the role of metal/oxide interfaces in the formation of oxygen vacancies. *ACS Catal.* **2017,** *7* (10), 6493-6513.

5. Mars, P.; van Krevelen, D. W. Oxidations carried out by means of vanadium oxide catalysts. *Chem. Eng. Sci.* **1954,** *3*, 41-59.

6. Misono, M., Heterogeneous Catalysis of Mixed Oxides: Perovskite and Heteropoly Catalysts. Elsevier, Newnes, U.K., 2013.

7. Rodriguez, J. A.; Kim, J. Y.; Hanson, J. C.; Pérez, M.; Frenkel, A. I. Reduction of CuO in H_2: in situ time-resolved XRD studies. *Catal. Lett.* **2003,** *85* (3-4), 247-254.

8. Kim, J. Y.; Hanson, J. C.; Frenkel, A. I.; Lee, P. L., Reduction of CuO and Cu_2O with H_2: H embedding and kinetic effects in the formation of suboxides. *J. Am. Chem. Soc.* **2003,** *125*, 10684-10692.

9. Yang, F.; Choi, Y.; Liu, P.; Hrbek, J.; Rodriguez, J. A., Autocatalytic reduction of a Cu_2O/Cu(111) surface by CO: STM, XPS, and DFT Studies. *J. Phys. Chem. C* **2010,** *114*, 17042–17050.

10. Goniakowski, J.; Noguera, C., Insulating oxide surfaces and nanostructures. *C. R. Phys.* **2016,** *17* (3), 471-480.

11. Renaud, G., Oxide surfaces and metal/oxide interfaces studied by grazing incidence X-ray scattering. *Surf. Sci. Rep.* **1998**, 32 (1), 5-90.

12. Zhu, Y.; Wu, D.; Liu, Q.; Sadowski, J. T.; Zhou, G. Hydrogen-induced clustering of metal atoms in oxygenated metal surfaces. *J. Phys. Chem. C* **2019,** *123* (18), 11662-11670.

13. Xu, F.; Mudiyanselage, K.; Baber, A. E.; Soldemo, M.; Weissenrieder, J.; White, M. G.; Stacchiola, D. J. Redox-mediated reconstruction of copper during carbon monoxide oxidation. *J. Phys. Chem. C* **2014,** *118* (29), 15902-15909.

14. Sha, H.; Liang, S.; Liu, L.; Cheng, Z.; Zhu, J.; Yu, R. Surface termination and stoichiometry of $LaAlO_3$(001) surface studied by HRTEM. *Micron* **2020,** *137*, 102919.

15. Liu, S.; Liu, L.; Cheng, Z.; Zhu, J.; Yu, R. Surface structures of Mn_3O_4 and the partition of oxidation states of Mn. *J. Phys. Chem. Lett.* **2021**, *12*, 5675-5681.

16. Huang, X. et al. Phase coexistence and structural dynamics of redox metal catalysts revealed by operando TEM. *Adv. Mater.* **2021,** *33*,2101772.

17. Newsome, D. S., The water-gas shift reaction. *Catal. Rev.: Sci. Eng.* **1980,** *21* (2), 275-318.

18. Klier, K., Methanol synthesis. *Adv. Catal.***1982**, *31*, 243-313.

19. Poreddy, R.; Engelbrekt, C.; Riisager, A., Copper oxide as efficient catalyst for oxidative dehydrogenation of alcohols with air. *Catal. Sci. Tech.* **2015,** *5* (4), 2467-2477.

20. Zhang, K.; Li, G.; Spurgeon, S. R.; Wang, L.; Yan, P.; Wang, Z.; Gu, M.; Varga, T.; Bowden, M. E.; Zhu, Z.; Wang, C.; Du, Y. Creation and ordering of oxygen vacancies at $WO_{3-\delta}$ and perovskite interfaces. *ACS Appl. Mater. Interfaces* **2018,** *10* (20), 17480-17486.

21. Hao, G.; Zhang, R.; Li, J.; Wang, B.; Zhao, Q., Insight into the effect of surface structure on H_2 adsorption and activation over different CuO(111) surfaces: A first-principle study. *Comput. Mater. Sci.* **2016,** *122*, 191-200.

22. Tu, K. N.; Yeh, N.; Park, S.; Tsuei, C., Diffusion of oxygen in superconducting $YBa_2Cu_3O_{7-\delta}$ ceramic oxides. *Phys. Rev. B* **1989,** *39* (1), 304.

23. Lawless, K. R. The oxidation of metals. *Rep. Prog. Phys.* **1974,** *37* (2), 231.

24. Carel, C.; Mouallem-Bahout, M.; Gaudé, J. Re-examination of the non-stoichiometry and defect structure of copper(II) oxide or tenorite, $Cu_{1\pm z}O$ or $CuO_{1\pm\epsilon}$: A short review. *Solid State Ion.* **1999,** *117* (1), 47-55.

25. Sun, X.; Zhu, W.; Wu, D.; Liu, Z.; Chen, X.; Yuan, L.; Wang, G.; Sharma, R.; Zhou, G. Atomic-scale mechanism of unidirectional oxide growth. *Adv. Funct. Mater.* **2020,** *30* (4), 1906504.